5-2017

High-redshift Blazars through NuSTAR Eyes

Lea Marcotulli
Clemson University, lmarcot@g.clemson.edu

HIGH-REDSHIFT BLAZARS THROUGH *NuSTAR* EYES

A Thesis
Presented to
the Graduate School of
Clemson University

In Partial Fulfillment
of the Requirements for the Degree
Master of Science
Astrophysics

---

by
Lea Marcotulli
May 2017

Accepted by:
Dr. Marco Ajello, Committee Chair
Dr. Dieter Hartmann
Dr. Bradley Meyer

Abstract

MeV blazars are the most powerful sources among the blazar class. With bolometric luminosities exceeding 10^{48} erg s^{-1} and powerful relativistic jets, they are usually detected at high-redshifts ($z > 2$) and they generally harbor extremely massive black holes ($M_{BH} \sim 10^9 M_\odot$). Being able to derive their physical properties such as jet power, accretion disk luminosity, bulk Lorentz factor of the jet (Γ) and black hole mass, enables us to put constraints in the understanding of this not well sampled class of objects and use them for example to probe the formation of massive black holes in the early universe.

In this thesis we have analyzed the broadband emission of three high redshift blazars, focusing on the high energy part of their spectral energy distribution. In fact, being able to obtain hard X-ray data from the recently launched *NuSTAR* and having γ-ray detections from the *Fermi*-LAT, we were able to constrain more accurately the high energy peak of their distribution and therefore more precisely infer their jet power, underlying electron distribution, Γ and viewing angle (θ_v). Gathering optical and UV data allowed us to determine the black hole mass of such powerful objects as well as their accretion disk luminosity.

This work has recently been published in ApJ (Marcotulli et al., 2017).

In Section 1, the broad family of active galactic nuclei (ANGs) and their main physical characteristics are introduced, with a focus on the subclass of blazars and specifically MeV blazars. In Section 2, the main instruments used in our research to gather and analyze data are described, with a particular interest on imaging in the hard X-ray regime. Section 3 contains the data analysis description, the results obtained combining the observations with a one-zone leptonic emission model and the discussion on our findings. In Section 4 we report our conclusions and present an outlook on future MeV blazars studies possibilities.

Appendix A, B and C contain an overlook of relativistic beaming, radiative processes and model used for these sources.

Acknowledgments

Being in Clemson has given me many satisfactions, and writing this thesis is one of them. But for this to be achieved, I needed the help of some fantastic people that deserve a proper thank you.

First Marco, my advisor, the best! Without you I wouldn't be here in the first place and I couldn't have had this great experience that has been living in the US. It's thanks to your advices and mentoring that I could do everything here and start my carreer. You made everything look easier and worth to. Plus, I mean, which advisor takes his students for camping? You're just great. Grazie infinatamente!

I also want to thank my unofficial advisor, Vaidehi. 'Handsome, smart, with a little bit of belly but no worries', not only you basically thaught me everything I know about blazars, but also about monkeys and you have been a good friend as well.

And thanks to our group: Aman, Abhishek, Stefano. Having your support makes everything easier and more fun.

I also want to thank all professors that have dealt with me in the first year.. and after: Dieter, Brad and Tewari. I learnt and I keep learning a lot from all of you.

I want to thank my friends in Clemson, that have become my family here throught these two years: Komal, Bipin, Subash, Prakash, P.K., Mihiri, Nick, Steve, Wren, Chuanchang. A particular thanks goes to Komal: without you I probably would have become crazy after the first few weeks of classes and teaching and I wouldn't have enjoyed all of this. You have been a friend, a sis and sometimes also a mom. There is no way I can be in Clemson without you. Then to all three bros: with our laughter and crappy jokes, it was possible to forget everything and to move on from every good or bad week. I love y'all so much!

And then of course there are all the people far away that have supported me since the first time I said I wanted to flea the country. Ma maman cherie adorée, that have always encouraged me for every choice in my life. My brother and my dad, that everytime something happens to me here, they spread the news in the whole Fermo. My friends, that even with 6 hours of time delay, always kept in touch as we were 5 minutes away and with whom I could swear in Italian everytime this town made me go nuts! Love, Mimmi, grazie!

To conclude I just want to say that I am grateful that I had this chance in my life. The chance to find a good advisor, good professors, and good friends. The chance to feel at home even being a non resident alien. And even if this is a small step, I know that many others will come in the next years. I love you all very much! Thank you!

Table of Contents

List of Tables

List of Figures

Chapter 1

Introduction

Active galaxies are a special type of galaxies whose emission is powered by accretion of gas onto central supermassive black holes. Some active galaxies are known to host powerful relativistic jets where particles are accelerated close to the speed of light and generate enormous amounts of electromagnetic radiation, from radio to γ-rays.

The sources in which these jets are aligned to our line of sight, are called blazars. Due to relativistic effects, the emitted radiation from blazars is Doppler boosted and therefore, these peculiar objects can be detected at large cosmological distances, allowing us to study the early Universe.

1.1 Historical background and Observational characteristics

While normal galaxies usually display an absorption spectrum, coming from the integrated light of all their stars, in 1909, Edward Fath for the first time detected some galaxies with emission lines coming from their center (Fath, 1909). In 1943, Carl Seyfert obtained the spectra from six bright galactic nuclei, located in what appeared to be normal spiral galaxies, and again saw that they contained broad emission lines (Seyfert, 1943).

Meanwhile, in the early 30's, at the Bell Telephone Laboratories Karl Jansky detected for the first time radio waves coming from outside the Solar System (Jansky, 1933). This discovery led scientists in the next decades

to start the development of radio telescopes, perform sky surveys and adopt interferometry to investigate this newly revealed cosmic emission (e.g. Reber, 1944; Southworth, 1945). All of this culminated in the 60's, with the discovery of the cosmic microwave background (CMB), pulsars and "quasi-stellar radio source", or quasars.

The nature of quasars remained unclear for a long time, due to the fact that their spectrum contained very peculiar features. As the name indicates, these sources, which when studied at radio wavelengths could have arcminute extension, in the optical range appeared as "point-like" objects, e.g. like a star. Even though the first quasar was discovered in the 50's, it took over ten years to obtain a definite identification of a radio source with an optical object (see, Greenstein & Matthews, 1963). When measured, the optical spectrum contained many unknown emission lines and the idea that quasars could have been extragalactic was not accepted for a while. Nonetheless it could not have been a star, as usually they show absorption lines. In 1962, thanks to its lunar occultation, the spectrum of another radio source, 3C 273, could be measured (Hazard et al., 1963) and again it showed broad emission lines. One year later, Maarten Schimdt realized that they were nothing less than hydrogen spectral lines highly redshifted (z=1.5, see, Schmidt, 1965). Therefore these objects were of extragalactic origin.

Another striking characteristic was the measured apparent magnitude of these sources ($m \sim 13$). The large distance combined with this m value implies a very large luminosity, which could not be explained by thermal processes (which power stellar emission). The idea that these sources could be powered by accretion onto a supermassive black hole (SMBH, $\gtrsim 10^8 - 10^9 M_\odot$) was hypothesized by Martin Rees in 1974 (Rees, 1974) and some times later the first indication of a SMBH in the center of our galaxy was detected (Balick & Brown, 1974).

The extended quasar radio emission was also a mystery for a long time. It was with the advancement of interferometry in radio astronomy that the instruments achieved a resolution of few tenths of milliarcseconds (e.g. Karl G. Jansky Very Large Array , VLA). This revealed the detailed structure of these powerful extragalactic radio sources. It became clear that they comprised two extended regions containing magnetic field and synchrotron-emitting relativistic electrons, each linked by a jet to a central compact radio source located in the nucleus of the associated galaxy (Begelman et al., 1984). Furthermore, the radiation was not homogeneous but was emitted from small blobs moving along the jets (e.g. Wehrle et al., 2001). Taking into account the large distance, the velocities of the blobs were calculated to be higher than the speed of light. Figure 1.1 shows the jet of M87: the right panel contains the sequence of images of the inner region of this jet

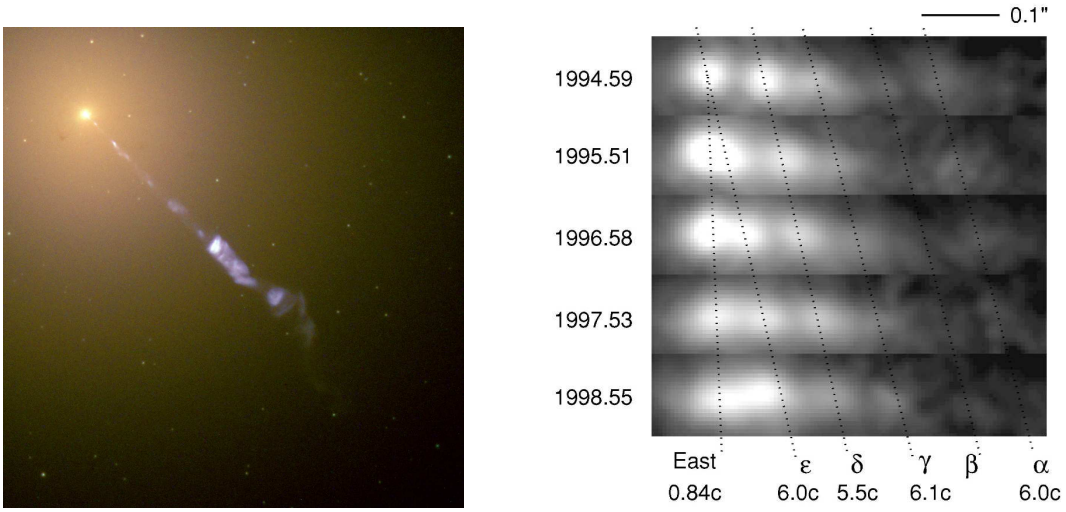

(a) (b)

Figure 1.1: Left panel (a): HST photograph of the relativitic jet ejected by M87 (credit:NASA and The Hubble Heritage Team, STScI/AURA). Right panel (b): sequence of the inner region of M87 jet, taken with the F342W filter ($\lambda = 342$ nm), between 1994 and 1998. The dotted lines attempt to indentify and follow features between the different epochs (Biretta et al., 1999). The apparent speed of these features is 6c.

which appears to emit features moving at 6c (Biretta et al., 1999). This effect, called superluminal motion, corresponds to proper fast motion (near the speed of light) of the spots happening at an angle close to the observer's line of sight (see Appendix A for further details).

It also became evident that a large fraction of quasars are actually radio-quiet, i.e. they emit no or little radio emission, while only a 15% of these objects have an abundant radio emission (radio-loud).

Another breakthrough came with the opening of the X-ray window in the 60s, first with rocket experiments led by Riccardo Giacconi and Bruno Rossi (see, Giacconi et al., 1962), then ten years later with the launch of the first X-ray satellites. These missions (like Uhuru, Ariel 5, HEAO-1 and Einstein satellites) revealed that quasars were also strong X-ray emitters. The idea started circulating that quasar were the main contributors to the cosmic diffuse X-ray background (discovered in 1962, see, Giacconi et al., 1962).

Even though X- and γ-ray astronomy commenced more or less at the same time, the impact of γ-rays on quasar research did not emerge as rapidly as the X-ray, due to the lower sensitivity of γ-ray telescopes compared to the X-ray ones. The first γ-ray measurement of a quasar (3C 273) was made by COS-B (Willmore, 1970) but it took other 20 years to obtain additional γ-rays detections thanks to the Compton Gamma-Ray

Observatory (CGRO, Gehrels et al. (1993)). With the advent of γ-ray detectors, some of these sources were discovered to emit γ-rays and also that their radiative output was dominated by this high-energy emission.

All these observational properties have been linked to a strong activity in the center of some galaxies. These are therefore called active galaxies and contain at their center an "Active Galactic Nucleus", or AGN. From the discovery of the first *Seyfert galaxies*, many classes of objects have been identified as belonging to the AGN family: Radio galaxies, Blazars, Quasi stellar objects (QSO, both radio-loud and radio-quiet), and Low ionization Nuclear Emission-Line Regions (LINERs). Despite the wide range of names and associated topologies, there exists a commonly accepted physical picture for these sources, as described in the following section.

1.2 Main AGN components

The current picture of AGNs ascribes the large luminosity coming from the central part of the hosting galaxy to accretion of matter onto a SMBH. Gas and dust surrounding the black hole are gravitationally attracted to it and form an accretion disk. Due to viscous processes and/or turbulence, this matter looses angular momentum in the accretion disk which, in return, highly increases its temperature and dissipates the extra energy emitting in the ultraviolet (UV) and X-ray frequencies in its inner regions and in the IR in the outer ones. The large amount of energy produced by the central accretion process influences the inner parts of the AGN (X-ray corona, broad and narrow line regions, as explained in the next sections) which then contribute to the broadband emission of such objects (from radio to γ-rays).

As already mentioned, a small percent of such sources is found to produce large scale radio structures, called jets, extending in opposite directions from the black hole. It is widely accepted that the plasma in the vicinity of the SMBH is accelerated and collimated by the lines of a magnetic field. In fact, neither gas nor radiation pressure appears to be adequate to collimate large momentum flux. The origin of this magnetic field though is not well understood (see Pudritz et al., 2012, for review). Generally, two scenarios are considered: a poloidal magnetic field threading the accretion disk (as described in Blandford & Payne, 1982) and/or a spinning black hole with a toroidal magnetic field threading its ergosphere (Blandford & Znajek, 1977). Most theories and simulation suggest that the spinning black hole would be responsible for producing the highly relativistic jets, while lower speed outflows would be driven by the surrounding disk. While gas flows radially inward

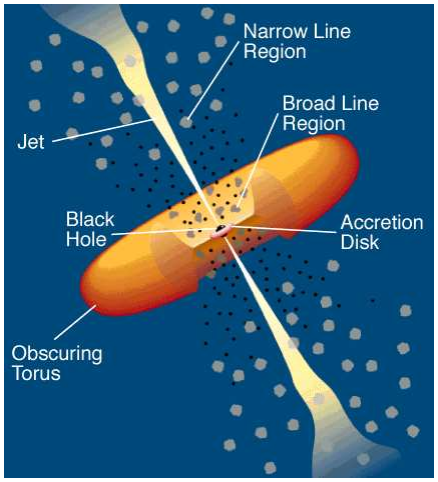

Figure 1.2: A schematic of an AGN with relativistic jets. At the center resides the SMBH surrounded by the accretion disk. Close to the SMBH, fast orbiting clouds of dust and gas produce broad lines (BLR). Farther away another region of clouds is found producing narrow lines (NLR). Some parsecs away from the SMBH sits the doughnut shaped torus (Urry & Padovani, 1995).

through the disk, it liberates energy and angular momentum that then is extracted by the jets. Hence, the transfer of energy powering the outflow is driven by conversion of gravitational energy into kinetic rotational energy and subsequently into an outflow that carries the energy in the form of kinetic jet power. How the conversion from gravitational to kinetic and radiative energy happens, though, is poorly understood. Furthermore, there is no widely accepted mechanism to explain the acceleration in this structure. The two leading theories assert that it is either due to diffusive shocks acceleration or to magnetic reconnection (see, Sironi et al., 2015, for further details). In Figure 1.2 we show the accepted schematic for an AGN.

1.2.1 Evidences for the existence of nuclear supermassive black hole

It was obvious till the first AGN detection that the powerful energy outflow could not have been driven by thermonuclear reactions, but was more likely related to gravitational energy and implied the existence of a SMBH. Some of the main observational evidences supporting the presence of a SMBH are the following:

- Given the luminosity of a quasar, assuming that stars are responsible for this nuclear emission and the efficiency of thermonuclear reactions is 1%, this would require a billion solar masses to be packed in a volume size not larger than our Solar System. In this situation, the gravitational binding energy would equal or exceed the nuclear energy therefore collapsing into a SMBH (Rees, 1984).

- Direct evidence of BH in AGNs has come from observations of mass and gas and stars in the vicinity of the BH. In the case of our own Galaxy, velocity dispersion measurements of stars within the nucleus have led to determination of a dynamical central mass of $\sim 10^6 M_\odot$ within a volume of radius 0.01 pc (e.g., Ghez et al., 1998). Hubble Space Telescope (HST) Measurements of the velocity field of hydrogen gas in active galaxies also indicates the presence of centrally condensed objects (e.g., Kormendy & Richstone, 1995).

- Superluminal motion observed in the radio structures of some sources implies velocities close to the speed of light. This plasma needs to be accelerated by an extreme source of energy at the center.

- If the gas surrounding a BH would accrete through Bondi accretion (steady, spherical symmetric accretion), it would not release all the thermal energy required to reproduce the measured high luminosities. It is more likely that the gas has an initial angular momentum and therefore collapses into a disk shaped structure that can radiate more efficiently (see Beckmann & Shrader, 2012).

  The HST observation of M87 directly showed the existence of an ionized disk rapidly rotating about the central part; the velocity measurement agrees with the disk being Keplerian with velocities $\sim 5 \times 10^7$ cms^{-1}. This high velocity is the mark of a huge gravitational field at the center of the galaxy and requires the existence of a SMBH, as a mass of $\sim 3 \times 10^9 M_\odot$ should be confined in a region no larger than our Solar System [1].

1.2.2 The accretion disk

In the accepted model for AGN, the central black hole is fed through an accretion disk. Both low and high accretion regimes (i.e., $L_{\rm disk}/L_{\rm Edd} \lesssim 10^{-2}$ and $L_{\rm disk}/L_{\rm Edd} \gtrsim 10^{-2}$, respectively, where $L_{\rm Edd}$ is the Eddington luminosity, Sbarrato et al., 2012) have been investigated by different models. Generally, for high accretion rates the most accepted scenario is the one of a geometrically thin, optically thick accretion disk (Shakura & Sunyaev, 1973). According to this model, following the pull from the central black hole, matter moves in a quasi-Keplerian orbit and approaches the center of the disk by loosing angular momentum through dissipative processes such as turbulence or friction. The disk radiation is approximated as a multi-color black body whose emission peaks around optical-UV frequencies. In the most powerful quasars usually it is possible to detect this emission and it is referred as the 'big blue bump' (see, Shields, 1978).

[1] The original press releas can be found at http://archive.seds.org/hst/M87Plot.html

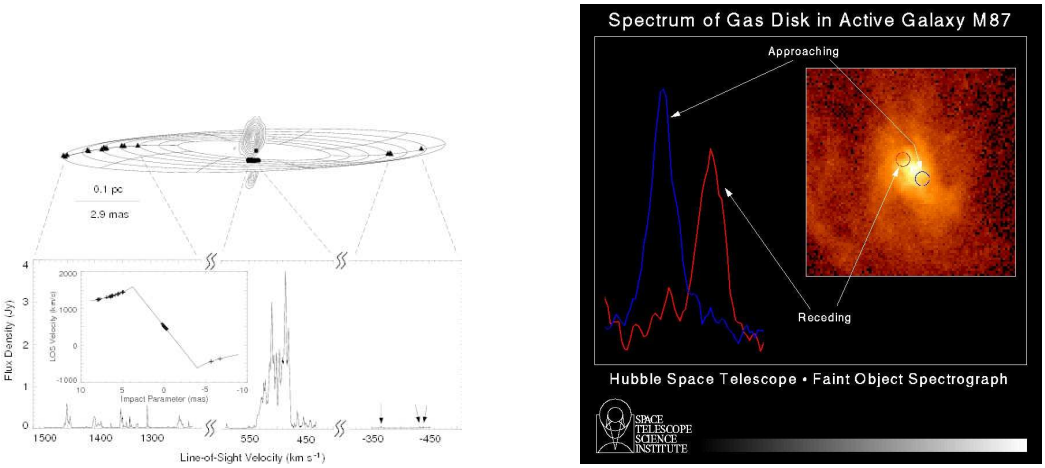

(a) (b)

Figure 1.3: Left panel (a): schematic drawing of the Keplerian disk surrounding a black hole as traced by maser measurements (black triangles) superposed with a radio frequency image (*contours*) of synchrotron emitting plasma jets emanating from the center of NGC 4285 with an observed spectrum (flux density versus Doppler velocity). *Inset:* Plot of maser Doppler velocity versus distance from the center. A Keplerian ($v \propto 1/\sqrt{r}$) rotation curve is shown with the curved solid lines. The straight line shows the changing line of sight projection of masers from the center of the spectrum that lie on a fixed radius in a small arc in front of the disk center. Right panel (b): HST observation of the ionized disk at the center of M87 with a schematic diagram of velocity measurements.

The disk is sandwiched by a corona of hot material which reprocesses the radiation from it Compton-scattering it up to X-ray energies.

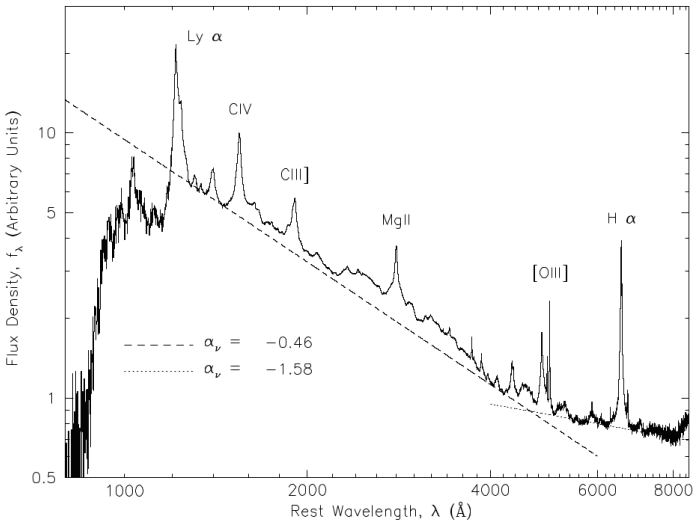

Figure 1.4: Composite quasar spectrum from optically-selected quasars in the Sloan Digital Sky Survey (SDSS, Vanden Berk et al., 2001). Broad and narrow lines are present. Note the precence of the forbidden [OIII] narrow line.

1.2.3 Broad Line Region

One interesting characteristic of AGNs is the emission lines in their optical spectra. These features can be either broad or narrow and are understood to originate from different locations of the AGN (see Figure 1.4). The broad line region (BLR) is believed to be composed by clouds of dust and gas located relatively close to the black hole ($\leq$ 0.1-1 pc). They are ionized by the radiation coming from the accretion disk and produce strong emission lines by recombination. Due to their closeness to the black hole, they move very fast producing Doppler broadening of the lines. Examining the optical spectra, the velocity of the clouds have been estimated around $10^3 - 10^4$ km s^{-1}, which is an indicator of the distance of these clouds from the central engine. As they reprocess the light from the accretion disk, the line luminosities are good tracers of the ionizing luminosity of the disk, hence of its overall luminosity. The density of these region is estimated to be $\sim 10^9 - 10^{11}$ cm^{-3} with a temperature of about 10^4 K, both properties derived by the presence or absence of some lines.

1.2.4 Narrow Line Region

The narrow line region (NLR) is similar to the BLR: made of clouds of gas and dust, it reprocesses the light from the accretion disk producing narrow line feature in the optical spectrum. Due to the width of the line, these regions are estimated to be farther away from the black hole, therefore moving at a lower velocity. They are located about $\sim$ 100 pc away and have velocities of the order of $\sim$ 100-500 km s^{-1}. The NLR lines are clearly distinguished by the ones produced by the BLR not only for their width but also for the fact that some are "forbidden" lines. The precence of these features is a tracer of the density of these regions: in fact above a critical density, the collisions are the main dominant factor for electron de-excitation, while below this density emission is possible. The density of the NLR is estimated $\sim 10^3$ cm^{-3} and temperatures are similar to the BLR.

1.2.5 Dusty Torus

Some AGNs were seen only showing narrow lines. Once analyzed in polarized light though the broad lines also appeared (see, Antonucci, 1993). Therefore there had to be an unpolarized continuum hiding them in

total light. The accepted idea is that at some parsec away from the black hole ($\sim$ 1-10 pc) lies a dusty molecular torus that obscures the central regions, and an observer looking at the AGN from the side would not be able to see the emission from the BLR. The torus absorbs the radiation coming from the center and re-emits it in the infrared (IR, see Figure 1.5). The polarization of the BLR emission is due to the presence in the central regions of free electrons that can scatter the disc and broad line emission, allowing the observer to see the fraction of this reprocessed light in polarized light. As for the structure of the torus, it is now widely accepted that it is made of clumpy distribution of dusty clouds (Nenkova et al., 2002).

1.2.6 The relativistic jets

About $\sim$10% of the AGN exhibit a prominent radio emission. This is produced by relativistic jets expelling matter from the black hole in opposite directions. Following the lines of the strong magnetic field piercing the accretion disk, energetic particles are accelerated near the speed of light and emit a copious amount of radiation. The relativistic speed can be inferred by the superluminal motion of the entire radio structure. The size of this object can achieve Mpc scales (10-100 times larger than the host galaxy) and in some sources giant radio structures are found at the end of the jets (see Figure 1.5). Those are referred as radio lobes and they are positioned where the jets decelerate due to interaction with surrounding matter. The process that launches these jets is not well understood and still a matter of debate. The leading theories asserts that it is due to electromagnetic extraction of energy and angular momentum from the accretion disk and rotational energy from the spinning SMBH (see, Blandford & Payne, 1982).

1.3 Unification

The AGN phenomenon was first defined based on observation characteristics: optical spectrum, radio emission, optical counterparts and so forth. Thus, since 1943, a large number of AGN types were discovered. From then, a big effort has been made to try to unify these separate subclasses. Two major classes have been established: radio-loud and radio-quiet source. This division is based on a parameter called the *radio-loudness factor* (R):

$$R = \frac{f_{5GHz}}{f_B} \tag{1.1}$$

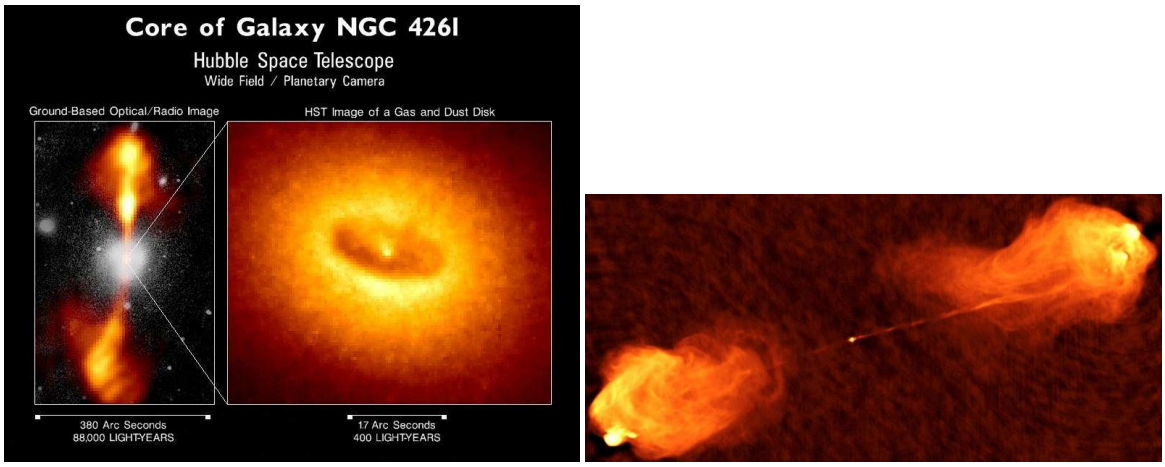

(a) (b)

Figure 1.5: Left panel (a): HST direct observational evidence of the dust torus around the centre of the radio galaxy shooted from the central galaxy at relativistic speed. At the end bright spots are evident (image courtesy of NRAO/AUI).

Table 1.1: Table of AGN subclasses

Radio Properties	Type 1	Type 2
Radio quiet	Seyfert 1	Seyfert 2
	QSO	
Radio Loud	BL Lac	FR I
	BLRG	NLRG
	Quasar/OVV	FRII

where f_{5GHz} is the flux density at 5 GHz and f_B is the flux density in optical B band ($\lambda = 4000\mathring{A}$). If R is greater than 10, the source is defined as radio-loud (Kellermann et al., 1989). It has been seen that only 10% of AGN are radio-loud, with emission dominated by the relativistic jets and their lobes.

Both radio-quiet and radio-loud are sub-classified as *Type 1* and *Type 2* objects depending on the the strength of the optical emission lines in their spectrum. *Type 1* AGN exhibit both broad and narrow emission lines while *Type 2* spectrum is mainly dominated by narrow lines. Other subclasses are summarized in Table 1.1.

The presence of an obscuring torus suggested that depending on the viewing angle of this obscuring material, different characteristic would appear in the spectrum of an AGN.

Another selection effect comes from the high anisotropy of AGN radiation. The jets moving at relativistic speed produce a strongly Doppler boosted radiation along their axis, hence effects such as relativistic beaming and superluminal motion can alter the appearance of these sources as well. Looking closer to the powerful ra-

dio jet, the luminosity would be amplified by the relativistic beaming, would appear more variable, polarized and show superluminal motions.

The idea for unification came when it was realized that one major factor could influence the aspect of these objects: orientation (Antonucci, 1993). Depending on the viewing angle, an observer looking an AGN face-on would detect the emission of the jet (if the object is radio-loud), see the NLR and BLR as well as the central engine with the accretion disk. An observer having an edge-on perspective would instead intersect the dusty torus on his line of sight so that the central region would be obscured and, at large angles, also the BLR would be hidden explaining the presence of narrow lines only.
This simple model, though explaining many observational differences between different AGN classes, has its own downfalls as for example it leaves a major open question about the difference between radio-loud and radio-quiet quasar.

According to the current unification model (Urry & Padovani, 1995), the class of radio-loud AGNs incorporates: radio-loud quasars, BL Lacertae objects (BL Lacs) and Flat Spectrum Radio Quasars (FSRQs) which all together are referred as blazars, narrow line radio galaxies (NLRGs) and broad line radio galaxies (BLRGs). Blazars are observed close to the line of sight of the observer, BLRGs and radio-loud quasar at modest angles and NLRGs at large angles. The class of radio-quiet objects contains: Seyfert Galaxies, radio-quiet quasars and LINERs. Figure 1.6 shows the basic schematic of the unification.

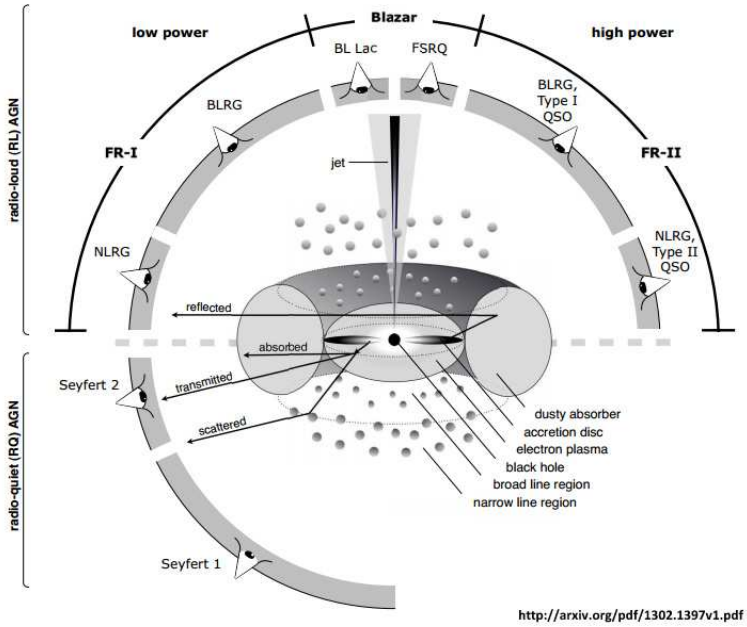

Figure 1.6: A schematic representation of the current understanding the AGN unification scheme. The upper part shows the radio-loud AGN while the lower part the radio-quiet (Beckmann & Shrader, 2012).

1.4 Blazars

Some AGNs are found to be radio-loud even though their radio emission cannot be resolved. Albeit true compact objects have been observed, most of these sources show peculiar spectral features that are ascribed to presence of a relativistic jet closely aligned to the line of sight of the observer. In fact they have a compact radio morphology with flat radio spectra ($\alpha_r < 0.5$, $F_\nu \propto \nu^{-\alpha_\nu}$; Urry & Padovani, 1995), as well as polarized and highly variable emission. These sources are collectively known as blazars. They are typically hosted in the nuclei of giant elliptical galaxies (Falomo et al., 2000; O'Dowd et al., 2002).

From their optical properties, they have been sub-classified as flat spectrum radio quasars (FSRQs), if their spectrum shows broad emission lines (equivalent width, EW$>$ 5Å), and BL Lacertae (BL Lac) objects which show weak (EW$<$ 5Å) or absent emission lines (Stickel et al., 1991; Stocke et al., 1991). This observational characterization could be related to different accretion mechanisms. The engine producing the ionizing radiation of these clouds is the accretion disk, therefore different accretion regimes would produce different emission lines strength. Efficiently accreting disks would produce high luminosities, hence the BLR would produce extremely luminous emission lines. Radiatively inefficient disks instead would not induce the BLR to produce broad emission lines (see, Begelman, 2014, for a detailed discussion). Considering the EW as a

good measure of line emission dominance over the underlying continuum, a classification based on it could correspond to an effective difference between the two sub-classes.

Blazars are known to radiate over the entire electromagnetic spectrum, from the low-energy radio band to very high-energy γ-rays. This radiation is primarily due to non-thermal emission processes and is believed to be the manifestation of a powerful relativistic jet (e.g., Blandford & Rees, 1978; Dermer & Giebels, 2016; Urry & Padovani, 1995).

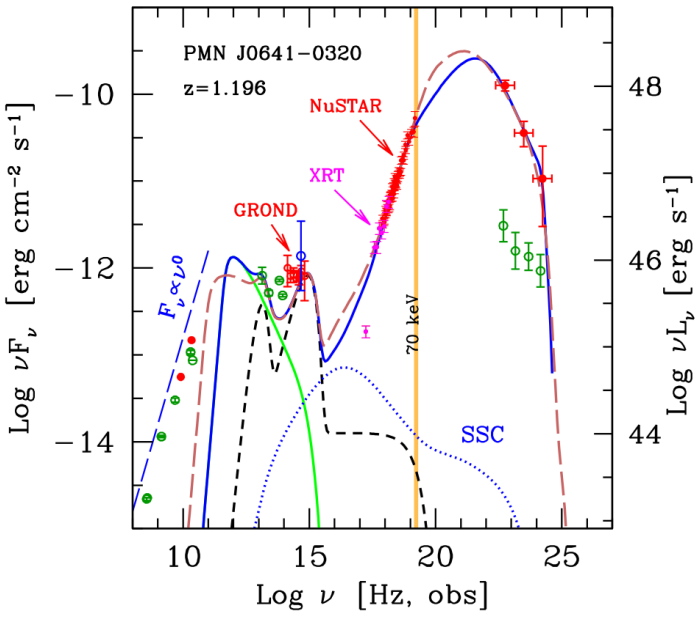

Figure 1.7: Typical SED of a blazar (adapted from Ajello et al., 2016): the low-energy hump is attributed to the synchrotron emission of the jet relativistic electrons, while the high energy hump is due to IC process of the same electrons with an external photon field.

The spectral energy distribution (SED) of a blazar displays two characteristic broad humps (see Figure 1.7), one peaking between infrared (IR) and X-ray frequencies and the other between the X-ray and γ-ray energy bands. The low-energy hump is understood as due to the synchrotron process of relativistic electrons present in the jet, supported by the observation of high degree of polarization. The high-energy peak instead is thought to be associated with inverse Compton (IC) scattering of low-energy photons by relativistic electrons. The majority of models agree on the fact that the population of electrons producing both peaks is the same (one-zone leptonic model). The low-energy photons can be either synchrotron photons (synchrotron self Compton or SSC; Konigl, 1981) or photons originating externally to the jet (external Compton or EC; Begelman & Sikora, 1987). In the SSC scenario, synchrotron photons are scattered by the same electrons that emit them. For EC,

the seed of photons reside outside the jet. This could be the accretion disk (e.g., Dermer & Schlickeiser, 1993), the BLR (e.g., Sikora et al., 1994) and/or the dusty torus (e.g. Błażejowski et al., 2000). As one process does not exclude the other, both are thought to be active even though their contribution is different for various blazars subclasses. As an example, FSRQs show a prominent thermal component (the 'big blue bump') that can act as a reservoir for EC process, thus are more likely to be dominated by EC high-energy emission. On the other end, BL Lac objects do not show any evident thermal emission. Lacking this external source of photons, most likely their γ-ray emission is produced mostly by SSC alone.

The Energetic Gamma-Ray Experiment Telescope (EGRET, Thompson et al., 1993), allowed scientist to discover that blazars emit most of their energy in the γ-ray band. After the launch of the Fermi-Large Area Telescope (*Fermi*-LAT, Atwood et al., 2009) it also became apparent that these sources are the strongest contributors to the extragalactic γ-ray background (Ajello et al., 2015). Therefore, γ-ray emission seems to be another peculiarity of blazars.

Another observational division between FSRQs and BL Lacs is that the former exhibit higher bolometric luminosities and lower peak frequencies than the latter. This anti-correlation between peak energies and luminosities is referred to as 'blazar sequence' (Fossati et al., 1998; Ghisellini et al., 1998, see Figure 1.8). A possible explanation can be related to intrinsic difference between FSRQs and BL Lacs. As mentioned before, FSRQs show a prominent thermal emission which corresponds to a dense photon field surrounding the jet. This results in a strong cooling by EC of jet electrons, that loose their energy before attaining the highest frequency peak, though making them achieve the highest luminosities. BL Lacs on the other hand are extreme accelerators but do not have such a dense thermal photon field, hence electrons cool less efficiently and can achieve very high energies (peak at GeV-TeV frequencies), but cannot reach high luminosities. Based on the location of their high energy peak (rest frame frequency peak, ν_{sync}^{peak}), Abdo et al. (2010) have classified blazars as low ($\nu_{sync}^{peak} < 10^{14}$ Hz), intermediate (10^{14} Hz $< \nu_{sync}^{peak} < 10^{15}$ Hz) and high ($\nu_{sync}^{peak} > 10^{15}$ Hz) synchrotron-peaked (respectively LSP, ISP, HSP). It appears that *Fermi*-LAT detected FSRQs are LSP while HSP sources are mainly BL Lacs.

1.4.1 MeV blazars

According to the above mentioned 'blazar sequence', the efficiency of electron cooling due to IC increases with increasing source luminosity. Moreover, due to the peculiar orientation of the relativistic jet, relativistic

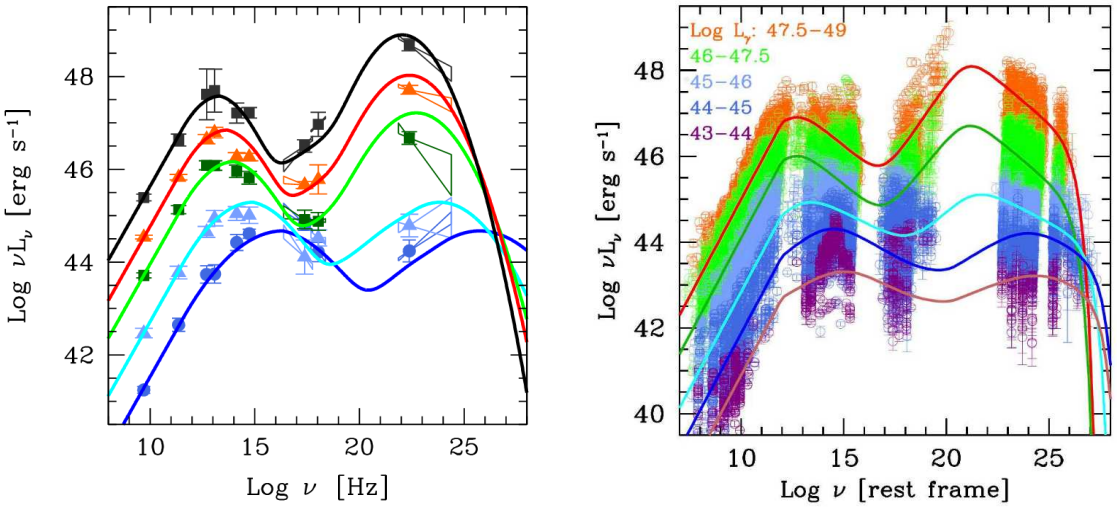

(a) (b)

Figure 1.8: Left panel(a): the original blazar sequence, constructed with the relatively few blazars belonging to complete (flux-limited) radio and X-ray samples of blazars (Fossati et al., 1998). Right panel: the new phenomenological sequence, obtained from all blazars with redshift detected by the Fermi satellite and listed in the 3LAC catalog (Ghisellini, 2016).

beaming plays a key role enhancing the source luminosity and thus enabling us to detect blazars at high redshifts. These arguments imply that the more distant and luminous the object is, the greater the shift of the SED humps towards lower frequencies.

The synchrotron peak of the most powerful blazars is located in the sub-millimeter (mm) range, while the IC peak falls in the MeV band (see Figure 1.9). The position of the latter classifies such objects as 'MeV blazars' (e.g., Bloemen et al., 1995). The characteristics of their spectra have allowed us to detect blazars up to $z \geq 5$ (e.g., Romani et al., 2004; Sbarrato et al., 2013).

MeV blazars are possibly the most extreme objects of this class:

- They typically have large bolometric luminosities ($L_{bol} > 10^{48}$ erg s^1)
- They host powerful relativistic jets ($P_j \geq \dot{M}c^2$ for a given accretion efficiency ; e.g., Ghisellini et al., 2014)
- In general they harbor extremely massive black holes ($M_{BH} \sim 10^9 M_\odot$; Ghisellini et al., 2010)
- They are usually found at high redshifts (z>2, Ajello et al., 2009).

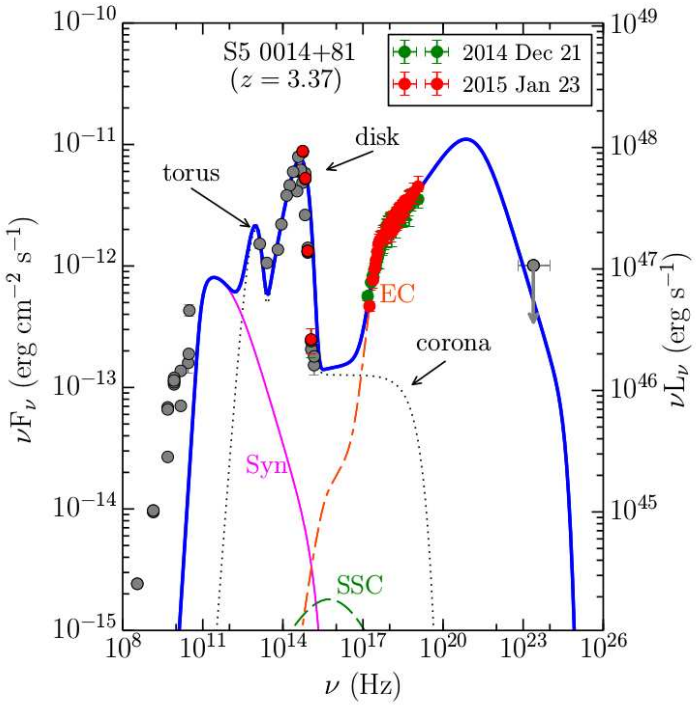

Figure 1.9: Example of SED of a high redshift blazar (Paliya et al., 2016).

The shift of the IC peak makes them bright at hard X-rays (> 10 keV) (see, e.g., Ghisellini, 2013b). Since the bolometric luminosity of blazars is dominated by high-energy emission (e.g., Ghisellini et al., 2014), an accurate measurement of the IC component in the SED provides important constraints on the power of the jet and on the relativistic particle population. With the advent of the first focusing hard X-ray telescope in orbit, the *Nuclear Spectroscopic Telescope Array* (*NuSTAR*; Harrison et al., 2013), it is now possible to explore the hard X-ray ($3-79$ keV) energy band with unprecedented detail and study the high energy emission of the most luminous and distant blazars with more accuracy.

Moreover, the shift in the synchrotron peak reveals the underlying optical-UV thermal emission from the accretion disk (e.g., Ghisellini et al., 2010). Modeling the disk emission it is possible to estimate the central black hole mass and the accretion disk luminosity. As a result, MeV blazars are ideal objects to study the accretion-jet connection.

Furthermore, these sources generally host extremely massive black holes at their centers. This has important implications as the detection of a blazar implies the existence of $2\Gamma^2$ such sources (where $\Gamma \sim$10-15, Γ being the bulk Lorentz factor of the jet, e.g., Sikora et al., 1997) with misaligned jets at the same redshift, hosting

similarly massive black holes (e.g. Ajello et al., 2009; Ghisellini et al., 2010).

Therefore a detailed study of MeV blazars, hosting extremely massive black holes, places useful constraints on the high end of the black-hole mass function, which is essential for a full theoretical understanding of the growth and evolution of black holes over cosmic time (e.g., Johnson & Haardt, 2016).

Despite being very interesting, unfortunately only a handful of bona-fide MeV blazars are known so far (e.g., Collmar, 2006; Sambruna et al., 2006). For every single MeV blazar, measurements of the bolometric, jet and accretion luminosity, together with Γ (given by the Compton dominance), the angle of the jet (given by the shape of the X-ray continuum) and the black hole mass are fundamental parameters to understand this source class and use them to (e.g.) probe the formation of massive black holes.

In this work, we have analyzed the broadband emission of three high-z MeV blazars. The requirement to study MeV blazars in the modes mentioned above (so to determine all those paramenters) is to have X-rays and γ-rays measurements of the IC peak. In fact, these sources have been selected as they are the only three sources, among the ten most luminous LAT FSRQs (Ackermann et al. 2015), which do not have hard X-ray coverage. Therefore we report their first E>10 keV detection obtained from NuSTAR observations. As such it becomes possible to accurately determine the location of the high-energy peak in their SEDs. Our primary motivation is to understand their physical properties by means of a multi-frequency data analysis and theoretical SED modeling, with a major focus on the hard X-ray observations. All three sources have been simultaneously observed by NuSTAR, Swift X-Ray Telescope (XRT; Burrows et al., 2005) and Swift-UltraViolet and Optical Telescope (UVOT; Roming et al., 2005). Thus, the X-ray energy band was fully covered from 0.3 up to 79 keV. To cover the infrared (IR) to ultra-violet (UV) part of the SEDs, we integrated the observations from Swift-UVOT with the ones from the Gamma-Ray Burst Optical/Near-Infrared Detector (GROND; Greiner et al., 2008); for two of the sources these were carried out within one week of NuSTAR observations, while for 3FGL J0453.2−2808 they were taken within six months, due to technical issues. We also analyze the recently released Pass 8 data from Fermi-LAT, which provides better sensitivity at lower energies (Atwood et al., 2013) compared to previously released datasets. Throughout, we use cosmological parameters $H_0 = 71$ km s^{-1} Mpc^{-1}, $\Omega_m = 0.27$, and $\Omega_\Lambda = 0.73$ (Komatsu et al., 2009).

Chapter 2

Facilities

Broadband studies are required in order to understand the physical properties of MeV blazars.
To cover the hard X-ray part, we used the recently launched Nuclear Spectroscopic Telescope Array (*NuSTAR*). Combined with simultaneous *Swift* X-ray Telescope (XRT) observations, the X-ray part of the spectrum was fully covered from 0.3 to 79 keV. Our three sources were also detected in γ-rays by the *Fermi*-Large Area Telescope (LAT). To cover the lower energy part of the spectrum we used the Gamma-Ray Burst Optical/Near-Infrared Detector (GROND) and *Swift* Ultraviolet and Optical Telescope (UVOT). The radio-IR data were extracted from the archive.

In this section we describe the main instruments used in our analysis. We focus our attention on hard X-ray imaging techniques and detectors, emphasizing the improvement of focusing telescopes (*NuSTAR*) with respect to collimated experiments and coded mask detectors.

2.1 Imaging in the hard X-ray regime

Photons of energies in the range 10-200 keV are defined as hard X-rays (by γ-ray astronomers). In this energy range, where Compton scattering does not fully overcome photoelectric absorption, both classical X-ray focusing techniques and Compton telescopes are difficult to use.
Till 15 years ago, the main technology adopted to detect hard X-rays (E$\geq$50-100 keV) from astrophysical

sources were either coded aperture telescopes or collimated experiments. The last decade has seen a major technological advance in the ability to focus hard X-rays. This has enabled the development of instruments orders of magnitude more sensitive compared to the previous technologies. Focusing telescopes have a significantly larger collecting area than the detector area used to register the signal. The large concentration factors for hard X-rays are favorable to improve the signal-to-noise ratio.

2.1.1 Collimated experiments and Coded mask detectors

Both collimated experiments and coded mask detectors are indirect techniques and have a common signature: the direction of the incoming radiation is encoded before detection. Therefore to obtain the image of the sky is necessary to reconstruct it by decoding the observation. These are referred as multiplexing techniques and differ from the direct imaging procedure of focusing techniques (see later). For non-focusing experiments, the detector area is approximately equal to the collecting area. As such, an imaged point source experiences the noise of all photons detected over the whole detector. The sensitivity of multiplex experiments is therefore worse than that of focusing telescopes, and a small signal to noise ratio can be achieved, which hampers the detection and study of faint X-ray sources.

Multiplexing techniques generally used are temporal and spatial. An example of temporal multiplexing is a scanning collimator: the direction of the collimator is moved across a part of the sky which contains an X-ray point source; the number of counts per second that is detected as a function of time has a triangular shape (see Figure 2.1). The position of the maximum of the triangle provides the position of the source along the scanning direction, and the height of the triangle provides the flux of the source. Another scan along another direction provides the the two-dimensional determination of the source. Examples of telescopes that used this technique are UHURU (Forman et al., 1978) and HEAO-1 (Wood et al., 1984).

Spatial multiplex instruments are in general referred to coded mask detectors. In these instruments, the incoming celestial radiation is modulated using a coded aperture, i.e. a plate which has different areas opaque or transparent to certain frequency ranges. A position sensitive detector, whose spatial resolution matches roughly the mask pattern grid size is used to record the modulated signal. The mask pattern is created in a way that ideally each source, at different positions in the field of view (FoV), casts a unique shadow on the detector plane. Therefore, the incident direction can be reconstructed from the count rates in the detector (see Figure 2.1).

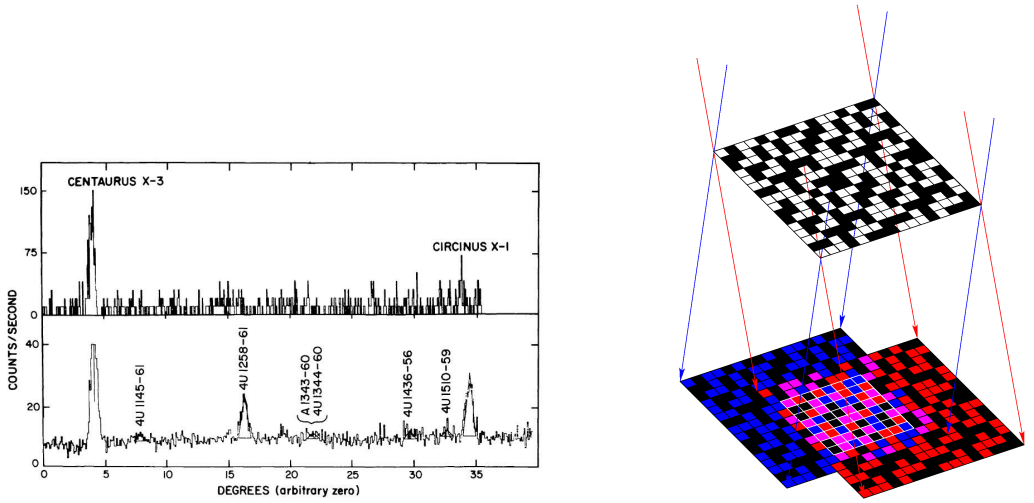

(a) (b)

Figure 2.1: Left panel(a): example of scanning collimator technique with a single scan of the galactic plane between Centaurus X-3 and Circinus X-l performed with UHURU (Forman et al., 1978); Right panel(b): schematic illustration of coded mask imaging with two sources in the sky (a red and a blue one), each projecting the mask pattern on the detector plane (credits: ISDC/M. Trler).

The geometry of the instrument determines both sensitivity (proportional to the opening factor, fraction of transparent and opaque mask elements) and angular resolution (ratio of transparent elements and distance of the mask above the detector plane). The constrain in angular resolution comes from the minimum dimension of a single detector (pixel) that should at least have a size comparable to a typical mask element to detect the shadowgram mask edges.

2.1.2 Focusing Telescopes

The preferred techinique to image hard X-rays would be a focusing telescope, similar to the ones used in optical astronomy. It represents a major improvement in sensitivity as it concentrates the source photons in a small area on the detector plane, therefore reducing by many orders of magnitude the background. Additionally, the ability to focus X-rays allows us to use small high-performance detectors, such as CCDs and calorimeters, not usually available for the large area configurations.

Total reflection for X-rays happens in the same way as visible light reflection. This radiation can experience total external reflection from surfaces positioned at very small grazing angle. Away from absorption edges

this angle is given by:

$$\theta_c \sim \sqrt{(}2\delta) \sim \frac{\sqrt{(}Z)}{E} \tag{2.1}$$

where $\delta = r_0 \lambda^2 N_e / 2\pi$, λ is the X-ray wavelength, r_0 is the classical electron radius and N_e is the electron density of the material.

The critical angle is inversely proportional to the energy. Thus higher energy photons require a smaller grazing angle in order to be totally reflected. This makes it more difficult to obtain large apertures at high energies. Also, θ_c is proportional to $\sqrt{Z}$, hence high-Z material are the preferred reflectors. The reflectivity is not a simple function of the photon energy though due to the presence of X-ray absorption edges in the surface material (see, Giacconi & Gursky, 1974, for a detailed explanation). Figure 2.2 shows different materials' reflectivity as a function of energy.

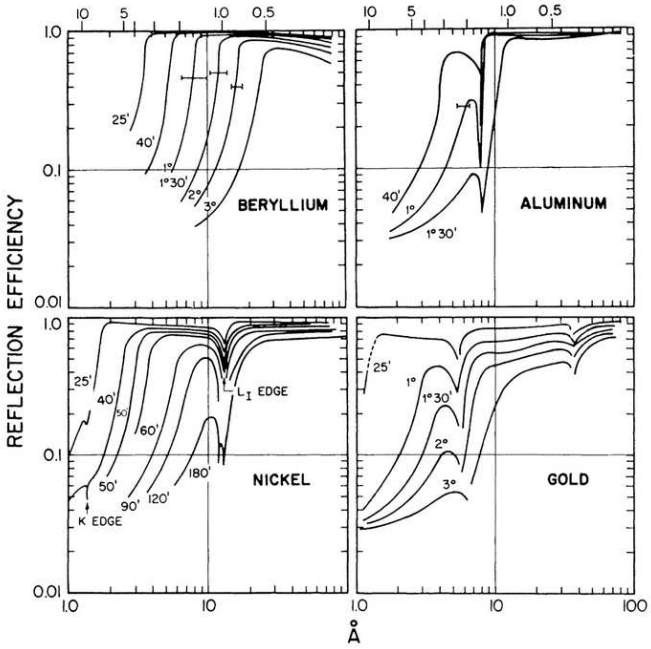

Figure 2.2: X-ray reflectivities plotted against wavelength for different materials and grazing angles (Zombeck, 1990).

Meeting all these criteria makes it possible to construct X-ray mirrors as focusing and imaging devices. Although reflection can be used, the fact that the grazing angle needs to be small implies a small effective reflecting area. This problem can be overcome by nesting reflecting surfaces: in this way a large effective area

can be achieved and both sensitivity and image quality increased with respect to non-focusing experiments. Using grazing incidence X-ray optics, in addition to a position-sensitive detector in the focal plane, allows us to achieve angular resolution at the level of arc seconds. The typical configuration of X-ray mirrors is the Wolter Type-1 mirrors, which is a combination of one parabolic and one hyperbolic surface. The incoming photons are first reflected by the parabolic mirror, which concentrates off-axis rays into an annulus. Then they are reflected by the hyperbolic one, which collapses the annulus in a point in the focal plane. To increase the effective area, several mirrors can be nested as shown in Figure 2.3.

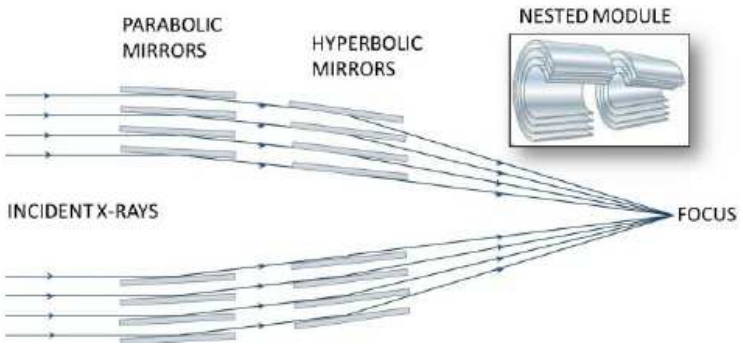

Figure 2.3: Schematic of an X-ray mirror with nesting of several surfaces.

2.1.3 X-ray detectors

In order to detect X-rays with E<100 keV, the detector absorbing material is chosen so that photoelectric absorption is the dominant effect. In this way, all the incident energy is collected in one point of the detector and it is possible to determine the incident energy as well as the event location. Photoelectric interaction frees charges that, once collected, may allow to determine interaction location, energy, polarization and arrival time of the incident X-ray.

These liberated charges can either be collected to generate an electrical signal at the output of the detectors or absorbed by calorimeters detector, thus producing a temperature gradient which is converted into an electrical signal. These electrical signals are subsequently amplified and processed to obtain the required information from the incoming radiation.

Most X-ray detectors use Charge-Couple Devices (CCDs) constructed with semiconductor materials. Semiconductors are preferred over solid state materials for their capacity to form information carriers such as

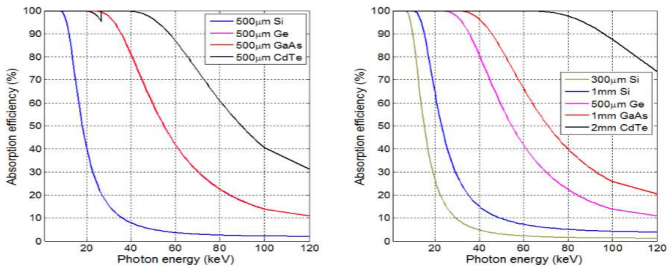

Figure 2.4: Absorption efficiency of different materials (Si, GaAs and CdTe) for different thicknesses (Ballabriga et al., 2016)

electrons or holes after the absorption of radiation. CCD arrays are a series of metal insulator semiconductor (MIS) capacitors that store the produced charge in their depletion region. Voltage differeces applied after collection allow the stored charge to flow from one capacitor to another. These detectors produce very low noise, have a high efficiency and a broadband usability (from Optical to X-ray), therefore they are the most used detector in astronomy.

Solid state detectors (see, Ballabriga et al., 2016) are also made of semiconductor materials (like silicon or germanium crystals). They consists of a p-n junction (i.e. an interface between two types of semiconductor materials, one "positive" side containing an excess of holes and one "negative" side containing an excess of electrons) which, once ionizing radiation strikes, develops a pulse of current. These pulses are amplified, recorded and analyzed in order to determine the energy, number or identity of the incident charged particles. A hybrid pixel detector is a 2-dimensional matrix of microscopic sensitive elements, each connected to its own readout electronics. The hybrid architecture allows the possibility to connect different semiconductor materials (Si, Ge, GaAs, CdTe or CdZnTe) to a readout ASIC, allowing system optimization. Radiation incident in the semiconductor detector produce electron-hole pairs (either by photoelectric absorption or Compton scattering; their number is proportional to the energy deposited) which are separated by an externally-applied electric field. The carriers drift and diffuse towards the electrodes, generating an electric current on the electrodes of the readout ASIC. Hybrid Pixel Detectors are attractive for X-ray imaging because: they allow direct detection, they treat individually the signal of each incoming photon and they allow optimal choice of sensor material for a given application. Nonetheless they have limitations like absorption efficiency or partial charge deposition due to fluorescence. A high quantum efficiency is required to detect photons of energies between 20 to 120 keV, hence high Z materials are to be employed. Figure 2.4 shows the absorption efficiency of four different materials for the same detector thickness and different thickness.

2.2 The Nuclear Spectroscopic Telescope Array

The *Nuclear Spectroscopic Telescope Array* (*NuSTAR*) mission is the first focusing high-energy X-ray telescope in orbit (Harrison et al., 2013) [1]. It covers the energy band from 3 to 79 keV, extending the sensitivity of focusing far beyond the $\sim$ 10 keV high-energy cutoff achieved by all previous X-ray satellites. The goal of the mission is to carry out high-sensitivity observations at X-ray energies significantly greater than 10 keV. It was launched on 13th June, 2012 from the Reagan Test Site on the Kwajalein Atoll in the South Pacific. It has a near-equatorial (6 degree inclination), low-Earth orbit ($\sim$600 km altitude).

NuSTAR consists of two co-aligned hard X-ray telescopes which are pointed at celestial targets by a three-axis stabilized spacecraft. It has a 10.14 m focal length. The science instrument uses the Wolter-I canonical approximation X-ray optics (Petre Serlemitsos 1985) consisting of two depth-graded multilayer-coated mirrors which focus onto two different solid state focal plane detectors at $\sim$ 10 m away from the optics. Both optics and detectors are designed in an identical way in order to produce focal plane images that can be added together and therefore improve the sensitivity.

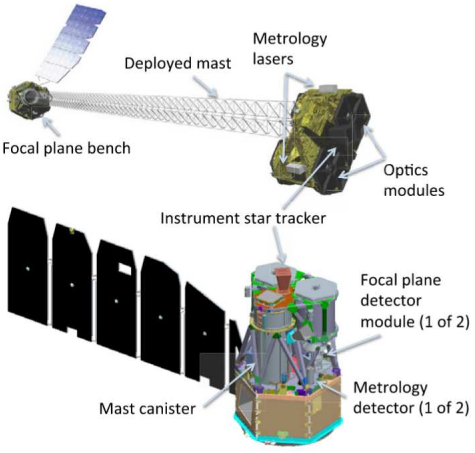

Figure 2.5: Diagram of the observatory in the stowed (bottom) and deployed (top) configurations.

Table 2.1: Table of *NuSTAR* optics parameters

Optics Parameters	Value
Focal Length	10.14 m
No. of shells	133
No. of azimuthal segments	6(inner)/12(outer)
Inner radius	5.44 cm
Outer Radius	19.1 cm
Shell length	22.5 cm
Min. graze angle	1.34 mrad
Max. graze angle	4.7 mrad
Coatings (inner)	Pt/C
Coatings (outer)	W/Si

The benches that support the optics and the focal plane systems are separated by a deployable composite mast. The stiffness of such a mast is not enough to maintain the required relative alignment of the benches in orbit, hence *NuSTAR* incorporates an aspect/metrology system. The latter consists of a star camera mounted

[1] Note: all Figures and Tables in Section 2.2 have been taken and/or adapted from Harrison et al. (2013)

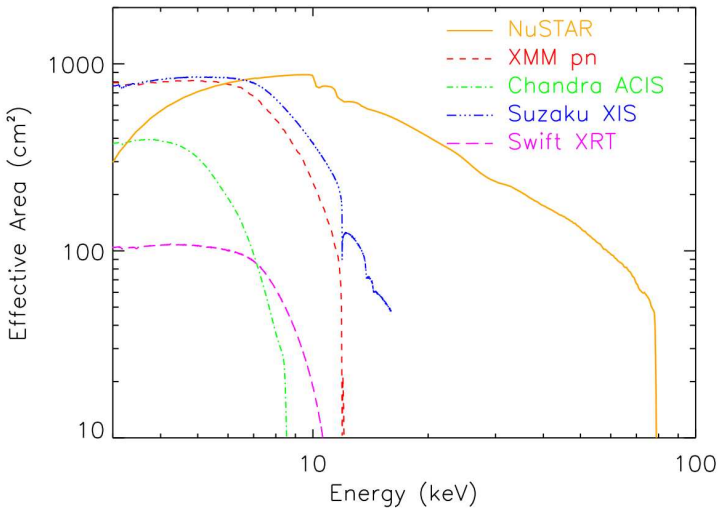

Figure 2.6: Effective collecting area of NuSTAR compared to selected operating focusing telescopes (*Chandra*, *XMM*, and *Suzaku*). *NuSTAR* provides good overlap with these soft X-ray observatories and extends focusing capability up to 79 keV (adapted from Harrison et al., 2013).

in the optics plane and two laser metrology units. Both these technologies combined are able to measure translation, tip, tilt and clocking between the benches. Using this information, it is possible to reconstruct the instantaneous instrument alignment and pointing direction. The measurements are combined on the ground during the data processing in order to remove blurring and determine correct response files.

As anticipated in Section 2.1.2, to focus hard X-rays *NuSTAR* utilizes of a low graze angle X-ray optics and multilayer coatings which combined enable a significant collecting area up to E$\sim$ 79 keV. The optics parameters are reported in table 2.1. Figure 2.6 shows the total effective area for both telescopes as a function of energy, with a comparison to operating focusing telescopes (Chandra, XMM-Newton, Suzaku).

The angular resolution of the instrument is dominated by the optics, and is $18''$ FWHM, with half power diameter of $58''$. The focal plane is designed to obtain good energy resolution (FWHM response 400 eV at 10 keV, 0.9 keV at 60 keV). An active anti-coincidence shield reduces background above 10 keV, so that overall the instrument detection threshold achieves more than two orders of magnitude improvement over collimated or coded aperture. The observatory performance parameters are listed in Table 2.2.

The focal plane of *NuSTAR* consists of two identical modules called FPMA and FPMB, each having four CdZnTe hybrid pixel detectors arranged in a two-by-two array. A picture of the focal plane is shown in Figure 2.7. A cylindrical active shield covers the detector array; it is made of cesium iodide (CsI) crystal coupled

Table 2.2: Table of Observatory Performance Parameters (adapted from Harrison et al., 2013)

Parameters	Value
Energy Range	3-78.4 keV
Angular Resolution (HPD)	$58''$
Angular Resolution (FWHM)	$18''$
FoV (50% resp.) at 10 keV	10'
FoV (50% resp.) at 68 keV	6'
Sensitivity (6-10 keV) (10^6 s, 3σ, ΔE/E=0.5)	2×10^{-15} erg cm^{-2} s^{-1}
Sensitivity (13-30 keV) (10^6 s, 3σ, ΔE/E=0.5)	1×10^{-14} erg cm^{-2} s^{-1}
Background in HPD (10-30 keV)	1.1×10^{-3} counts s^{-1}
Background in HPD (30-60 keV)	8.4×10^{-4} counts s^{-1}
Energy resolution (FWHM)	400 eV at 10 keV, 900 eV at 68 keV
Strong source ($> 10\sigma$) positioning	$1.5''(1\sigma)$
Temporal resolution	2μs
Target opportunity response	<24 hrs
Slew rate	$0.06^\circ s^{-1}$
Settling time	200 s (typ)

with a photomultiplier tube to discard the background using anti-coincidence. Each CdZnTe detector has a collecting area of 2cm $\times$ 2 cm and thickness of $\sim$ 2 mm. The ASIC of each detector contains an analog to digital converter and 1024 channels to amplify the signal and a discriminator to read it out. The main focal plane parameters are listed in Table 2.3.

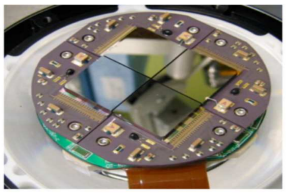

Figure 2.7: Photograph of a NuSTAR focal plane which consists of a 2×2 array of CdZnTe pixel detectors (adapted from Harrison et al., 2013).

Table 2.3: Focal Plane Parameters (adapted from Harrison et al., 2013)

Focal Plane Parameters	Value	Focal Plane Parameters	Value
Pixel size	0.6 mm/$12.3''$	Max. processing rate	400 events s^{-1} module^{-1}
Focal plane size	12' × 12'	Max. flux meas. rate	10^4 counts s^{-1}
Hybrid format	32 pix × 32 pix	Time resolution (relative)	2 μs
Energy threshold	2 keV	Dead time fraction (at threshold)	5%

2.3 *Fermi* Large Area Telescope (LAT)

The *Fermi* Gamma-ray space Telescope (*Fermi*) is a space observatory lauched by NASA on 2008 June 11 in a low Earth orbit and is used to study the entire sky at γ-rays.

Its primary instrument is the Large Area Telescope (*Fermi*-LAT, Atwood et al., 2009) [2]. This high-energy

[2]Note: all Figures and Tables in Section 2.3 have been taken and/or adapted from Atwood et al. (2009)

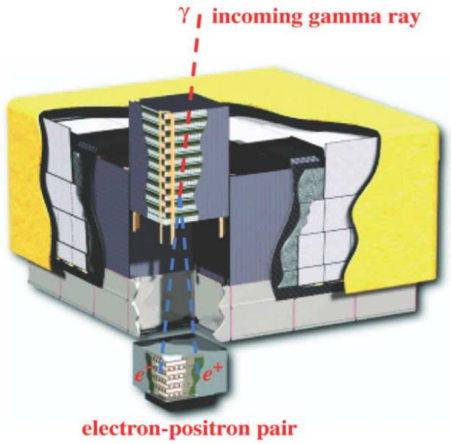

Figure 2.8: Schematic diagram of the *Fermi*-LAT instrument.

γ-ray telescope covers the energy range from $\sim$ 20 MeV up to $\geq$ 300 GeV. It is designed to measure the directions, energies and arrival times of γ-rays incident over a wide FoV (2.4 sr, $\sim$20% of the sky) and at the same time reject the background from cosmic rays.

Due to their high-energy, it is hard to reflect γ-rays. Instead in the interaction with matter they convert to an electron-positron pair (e^+e^-). The *Fermi*-LAT has been designed as a pair conversion telescope with a precision converter-tracker and calorimeter each consisting of 4x4 array of 16 modules supported by a low-mass aluminum grid structure. The converter-tracker is composed by 16 planes of high-Z converter material (tungsten) that produce the pair once a γ-ray photon hits the surface. These charged particles intersect interleaved layers of Si microstrip position-sensitive detectors causing ionization. This consequently produces detectable tiny electric pulses, thus permitting the measurements of the tracks of the particles resulting from the pair conversion. This information is used to reconstruct the direction of the incident radiation. After passing through the tracker, the particles enter the calorimeter. This is composed of a stack of Caesium iodide scintillator crystals which allows the measurement of the total energy of the particles.

A segmented anticoincidence detector (ACD) covers the tracker array. Its purpose is to provide rejection of charged-particle background, therefore its main requirement is to have a high detection efficiency (0.9997 for single charged particle detection). To form a trigger, the signals from the tracker, calorimeter and ACD subsystem are used by a programmable trigger and data acquisition system.

The processing onboard the LAT is optimized in order to reject events triggered by cosmic-ray background particles and at the same time to maximize the number of events caused by γ-rays, which are then trasmitted

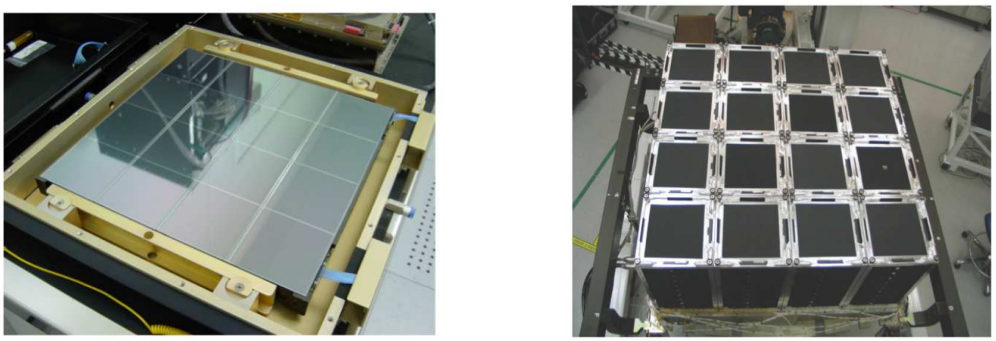

(a) (b)

Figure 2.9: Left panel(a): picture of the flight tracker tray. Right panel(b): picture of the completed tracker array before integration with the ACD (adapted from Atwood et al., 2009).

to the ground. The aspect ratio (height/width) of the LAT tracker is 0.4, allowing a large FoV and ensuring that nearly all events initiated in the tracker will reach the calorimeter. Table 2.4 contains the summary of the LAT instrument parameters and estimated performance.

Table 2.4: LAT instrument parameters and Estimated Performance (adapted from Atwood et al., 2009)

Parameters	Value
Energy Range	20 MeV-300 GeV
Effective area at normal incidence	9500 cm^2
Energy resolution (equivalent Gaussian 1σ):	
100 MeV-1 GeV (on-axis)	9%-15%
1 GeV-10 GeV (on-axis)	8%-9%
10 GeV-300 GeV (on axis)	8.5%-18%
$>$10 GeV ($>60^\circ$ incidence)	$\leq$6%
Single photon angular resolution (space angle)	
on-axis, 68% containment radius:	
$>$10 GeV	$\leq 0.15^\circ$
1 GeV	0.6°
100 MeV	3.5°
on-axis, 95% containment radius	$<3\times\theta_{68\%}$
off-axis, containment radius at 55°	$<1\times$ on-axis value
Field of view (FoV)	2.4 sr
Timing accuracy	$< 10\ \mu$s
Event readout time (dead time)	26.5 μs

2.3.0.1 Dataset

The filetypes obtained from the onboard processing coming to the ground are called 'Level 0' data. Subsequent processing involves the reconstruction of the event interaction in the LAT from the 'hits' (signals that result from the event interaction or its products with the various part of the LAT), identification of the event type (e.g. an astrophysical photon) and characterization of the event's relevant parameters (direction, energy). These are regarded as 'Level 1' data. [3]

Over the course of the mission, there have been improvements in understanding the performance of the satellite as well as the characterization of its environment. In order to take advantage of these developments, the LAT event-level analysis software has been periodically updated.
Since its launch, there have been four major data releases (Passes): Pass 6, Pass 7, Pass 7 Reprocessed, and Pass 8. The latest Pass 8 release has introduced significant changes to the event-level reconstruction with respect to the other Passes. Whereas the previous versions were primarily focused on reducing systematic uncertainties in the instrument response functions, Pass 8 is a comprehensive revision of the entire analysis chain that yields substantial gains in instrument performance.

Although originally motivated by the issue of ghost events (instrumental pile-up away from the gamma-ray shower), the new event reconstruction has brought many improvements such as:

- A new pattern recognition algorithm in the tracker reconstruction that does not depend on calorimeter information and is less sensitive to track confusion induced by the backsplash.
- A clustering stage in the calorimeter reconstruction aimed at finding and discarding the charge deposition due to ghost events.
- A better energy reconstruction that improves the handling of energy leakage and crystal saturation.
- A better algorithm for the association between tracks and ACD tiles for the rejection of charged particles.
- A new event classification analysis based on boosted decision trees that improves the separation power between photon and cosmic-ray background events.

[3] All informations contained in Section 2.3.0.1 can be found at http://fermi.gsfc.nasa.gov/ssc/data/analysis/documentation/

From the revision of the instrument Monte Carlo, new selection cuts have been generated which enhance the acceptance over the entire energy band of the LAT. The cut on the minimum energy deposited in the calorimiter has been removed with respect to Pass 7, hence significantly increasing the acceptance at lower energies (< 100 MeV).

Thanks to these improvements, Pass 8 contains many more events for a given time span than previous Passes. Even though this increase in effective area corresponds to an increase in the background levels, the signal-to-noise ratios also have improved so that the point source sensitivity of the LAT at all energies is boosted.

2.4 *Swift*

The *Swift* Gamma Ray Burst Explorer (Gehrels et al., 2004) is a NASA's MIDEX mission launched on 20 November 2004. The satellite carries on board three instruments: a Burst Alert Telescope (Barthelmy et al., 2005), which identifies gamma-ray bursts (GRBs) and determines their location on the sky to within a few arcminutes; an Ultraviolet/Optical Telescope (Roming et al., 2005) with limiting sensitivity of 24th magnitude in 1000 s and with 0.3 arcsecond position accuracy; and an X-ray Telescope (Burrows et al., 2005). It is a multiwavelength (coverage 0.2150 keV and 170600 nm) observatory dedicated to the study of Gamma-ray bursts (GRBs) and GRBs afterglow.

2.4.1 *Swift* X-ray Telescope

The *Swift*-XRT (Burrows et al., 2005) [4] is a soft X-ray focusing telescope, which covers the energy range from 0.2 to 10 keV. It utilizes grazing incidence, Wolter Type-I configuration mirrors that focus the incoming radiation into a thermally cooled CCD. The mirrors are the ones built and calibrated for the JET-X program (Citterio et al., 1996), composed by 12 concentric Ni shells with a gold coating. The focal length of the telescope is 3500 mm. The focused X-rays are collected by a CCD which is a copy of the EPIC-MOS instrument on *XMM-Newton* (e2v CCD-22 detector). The XRT is a sensitive ($2 \times 10^{-14}\,\mathrm{erg\ cm^{-2}\,s^{-1}}$ in 10^4s) broadband imager covering from 0.2 to 10 keV with an effective area >120 cm^2 at 1.5 keV, field of view of 23.6 $\times$ 23.6 arcminutes and angular resolution of 18 arcseconds (HPD). All instrument properties are

[4] Note: all Figures and Tables in Subsection 2.4.1 have been taken and/or adapted from Burrows et al. (2005)

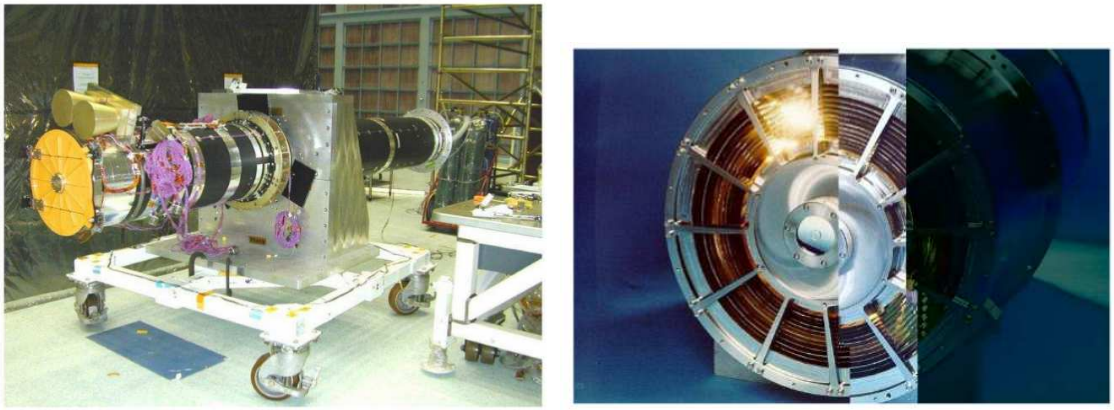

(a) (b)

Figure 2.10: Left panel(a): XRT installed in test cart before thermal vacuum tests in July 2002, with star tracker simulators installed. Right panel(b): XRT mirror module (adapted from Burrows et al., 2005).

listed in Table 2.5.

The instument works in an auto-exposure mode that automatically adjusts the CCD readout mode in order to obtain the optimized data for each frame. As the main aim of the mission is to measure fluxes, spectra and lightcurves of GRBs, XRT is designed in order to cover their rapid variability and dynamic ranges. It supports three readout modes: imaging, to produce an integrated image and measure the total energy per pixel; timing, to achieve high time resolution (2.2 ms) and spectroscopy even despite losing position informations; photoncounting mode, to obtain full spectral and spatial informations for source fluxes. It is designed to determine GRBs positions with an accuracy of few arcsec within $\sim$100s of the burst onset. It can also perform redshift measurements of the sources using the Fe emission line or other spectral features.

Table 2.5: XRT instrument parameters (adapted from Burrows et al., 2005)

Parameters	Value
Telescope	Wolter I
Focal length	3.5 m
Detector	e2v CCD-22
Detector format	600×600 pixels
Pixel size	40×40 μm
Field of View (FoV)	23.6×23.6 arcminutes
PSF	18 arcsec HPD at 1.5 keV
	22 arcsec HPD at 8.1 keV
Position Accuracy	3 arcsec
Time resolution	0.14 ms, 1.8 ms, or 2.5 s
Energy range	0.2-10 keV
Energy resolution	140 eV at 5.9 keV
Effective area	~ 125 cm ^{2} at 1.5 keV
	~ 20 cm ^{2} at 8.1 keV
Sensitivity	2×10^{-14} erg cm^{-2} s^{-1}in 10^4 s

Table 2.6: UVOT instrument parameters (adapted from Roming et al., 2005)

Parameters	Value
Aperture	30 cm diameter
f-number	12.7
Filters	11
Wavelength range	170-600 nm
Detectors	MCP Intensified CCD
Sensitivity	m_B=24.0 in white light in 10^3 s
Field of view	17×17 arcmin^2
Telescope PSF	0.9 arcsec FWHM at 350 nm

2.4.2 *Swift* Ultraviolet and Optical Telescope

The *Swift*-UVOT (Roming et al., 2005) [5] is a modified Ritchey-Chrtien reflector with a 30 cm primary mirror which covers the wavelength range from 170 to 600 nm. The optics used for the UVOT are the spares from the XMM-Newton Optical Monitor (OM). The telescope directs the incident light to one of the two detectors each lying behind an 11-position filter wheel which contain UV and optical grisms as well as broadband color filters. The detectors are micro-channel plate intensified CCD (MICs) that image the incoming photons operating in a photon counting mode. These detectors are also copies of the ones from the XMM OM design. As the background level in orbit is low, UVOT can detect a B-star of magnitude 24 in 10ks in white light. This instrument is coaligned with the XRT. It has a field of view of 17×17 arcmin^2 and a PSF of 0.9 arcseconds at 350 nm. Its main goal is to capture the UV and optical photons of the first ~ 1 min from the GRB afterglow

[5] Note: all Figures and Tables in Subsection 2.4.2 have been taken and/or adapted from (Roming et al., 2005)

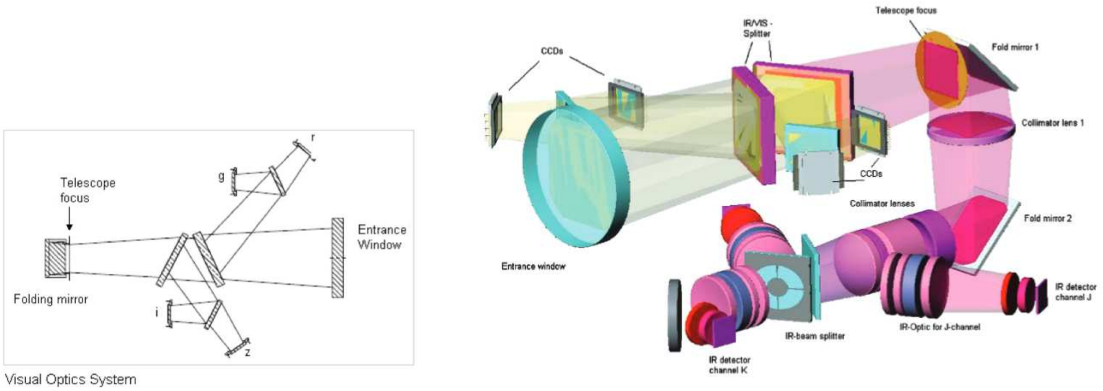

(a) (b)

Figure 2.11: Left panel(a): Layout of the of GROND optics showing a cut through the visual arm. Right panel(b):Visual and NIR beams 3D structure with most of the components labeled.

and can locate GRB's position to sub-arcseconds precision.

The main instrument characteristics are reported in Table 2.6

2.5 Gamma-Ray Burst Optical/Near-Infrared Detector

GROND (Greiner et al., 2008) [6] is a 7-channel imager whose primary mission is to identify GRBs afterglows and measure their redshift. This instrument is mounted on the MPI-owned 2.2 m telescope, on La Silla (Chile) and was commissioned in April 2007. The telescope is a Ritchey-Chretien of 17600 mm focal length and f/8.005 and intrinsic image quality 0.4″.

As GRBs afterglow fades in few minutes by $\sim$ 3 magnitudes and by other 4 mag in the next 50 min, in order to determine the photometric redshift it is necessary to use a multiband photometry in 3-4 bands. GROND allows simoultaneous imaging in the Sloan g' r' i' z' (354nm - 905 nm) and near-infrared JHK bands(1220nm -2190nm). For the visual channels, the incoming beam is split with four dichroics and reaches the detectors which are four backside illuminated e2v CCDs (20482$\times$13.5m size) which operates in inverted (AIMO) mode. Each CCD has a 5.4$\times$5.4 arcmin^2 field of view.

For the NIR, an optimized adjustment of the field of view is achieved with the focal reducer system design.

[6] Note: all Figures and Tables in Subsection 2.5 have been taken and/or adapted from Greiner et al. (2008)

This system is realized using 5 collimator lenses with a resulting $F_{coll} = 360$ mm and 6 camera lenses with $F_{cam} = 129.6$ mm for each NIR channel. The required 10' FoV is imaged by a Rockwell HAWAII-1 array of 1024×1024 pixels^2. The resulting effective focal length for the f=8 telescope is 6336 mm. The JHK filters have a reduced blicking range with respect to canonical NIR filters, which combined with the action of the dichroics achieve a 98% mean transmission in the J H K bands. A schematic of the optics is reported in Figure 2.11.

Chapter 3

MeV Blazars through Nustar Eyes

The most powerful sources among the blazar family are MeV blazars (see Chapter 1 for detailed discussion) [1]. In the present work we perform a multiwavelength study of three high redshift blazars: 3FGL J0325.5+2223 ($z = 2.06$), 3FGL J0449.0+1121 ($z = 2.15$), and 3FGL J0453.2$-$2808 ($z = 2.56$), analysing quasi simultaneous data from GROND, *Swift*-UVOT and XRT, *NuSTAR*, and *Fermi*-LAT (intruments descriptions can be found in Chapter 2). Our main focus is on the hard X-ray band recently unveiled by *NuSTAR* ($3-79$ keV) where these objects show a hard spectrum which enables us to constrain the inverse Compton peak and the jet power.

We found that all three targets resemble the most powerful blazars, with the synchrotron peak located in the sub-millimeter range and the inverse Compton peak in the MeV range, and therefore belong to the MeV blazar class. Using a simple one zone leptonic emission model (described in Appendix C) to reproduce the spectral energy distributions, we conclude that a simple combination of synchrotron and accretion disk emission reproduces the infrared-optical spectra while the X-ray to γ-ray part is well reproduced by the inverse Compton scattering of low energy photons supplied by the broad line region. The black hole masses for each of the three sources are calculated to be $\gtrsim 4 \times 10^8 M_\odot$. The three studied sources have jet power at the level of, or beyond, the accretion luminosity.

In Section 3.1 we describe the different data analysis techniques used for the different sets of data gathered

[1] This chapter has been extracted from the published Marcotulli et al. (2017)

from the various facilities. Section 3.2 highlights the main results from this work. Finally, Section 3.3 provides a thorough discussion of our results.

3.1 Observations

3.1.1 *Fermi*

The LAT Pass 8 data used in this work covers the period of *NuSTAR* observations. Since all three objects are faint in γ-rays, we chose a large time bin (MJD 57082$-$57448) to generate a meaningful SED. Moreover, there is no significant γ-ray variability detected from these sources[2], and therefore, the selected period is a reasonable choice.

We followed the standard data reduction procedure as given in the online documentation[3] with a few modifications. In the energy range 0.06$-$300 GeV, we only selected SOURCE class events (`evclass=128`), including all four point spread function (PSF) event types lying within a 15° region of interest (ROI) centered at the target source. We used a relational filter "`DATA_QUAL>0`", && "`LAT_CONFIG==1`" to define good time intervals. Only the events with zenith angle of 70°, 75°, 85° and 90° (according to the PSF types) were included in the analysis in order to avoid contamination from Earth-limb γ-rays. We performed a component-wise data analysis to account for different PSF types and considered the third catalog of *Fermi*-LAT detected sources (3FGL; Acero et al., 2015) to generate a source model. The source model includes all the sources present within the ROI, a Galactic diffuse emission component (gll_iem_v06.fits) and isotropic emission models (iso_P8R2_SOURCE_V6_PSF#_v06.txt, where #: 0, 1, 2, and 3) (Acero et al., 2016). A combined fitting was performed using the summed likelihood method included in the pyLikelihood library of the ScienceTools to derive the strength of the γ-ray signal. This was accomplished by computing a maximum likelihood test statistic TS = $2\Delta \log(\mathcal{L})$ where $\mathcal{L}$ represents the likelihood function, between models with and without a point source at the position of the object (Mattox et al., 1996). Since we were using data below 100 MeV, we enabled the energy dispersion corrections for all sources, except for the diffuse backgrounds. We performed a first round of optimization to obtain a best initial guess of the spectral parameters for all sources. We then allowed the spectral parameters of all the sources having TS$>$25 and lying within 10° from the center of the

[2]We searched for significant γ-ray flux variations using the tool '*Fermi* All-sky Variability Analysis' (FAVA; Ackermann et al., 2013), but found none, at least during the period covered in this work.

[3]http://fermi.gsfc.nasa.gov/ssc/data/analysis/documentation/

ROI to vary during the fitting. In the source spectra, only spectral bins where the source was detected with TS$>$9 are reported.

3.1.2 *NuSTAR*

The blazar 3FGL J0325.5+2223 was observed by *NuSTAR* on 2015 November 8 for a net exposure of 22.2 ks; 3FGL J0449.0+1121 was observed on 2015 December 2 for a net exposure of 20.5 ks; and 3FGL J0453.2−2808 was monitored on 2015 December 3 for a net exposure of 19.5 ks. The data for both *NuSTAR* Focal Plane Modules (FPMA and FPMB; Harrison et al., 2013) were processed using the *NuSTAR* Data Analysis Software (NUSTARDAS) v1.5.1. We calibrated the event data files using the task *nupipeline*, with the response file taken from the latest Calibration Database (CALDB). The generation of source and background spectra, ancillary and response matrix files, has been achieved using the *nuproducts* script. We selected circles with radii of 30″centered on the target sources as the source regions and the background events were extracted from circles with the same area but from a nearby source-free region on the same frame.

3.1.3 *Swift*

Swift-XRT (Burrows et al., 2005) and UVOT (Roming et al., 2005) observations were carried out simultaneously with *NuSTAR* monitoring. 3FGL J0325.5+2223 was observed on 2015 November 8, whereas 3FGL J0449.0+1121 and 3FGL J0453.2−2808 were monitored on 2015 December 2 and December 3, respectively. The exposure time for each of the three targets was $\sim$2 ks.

Due to these short exposure times and the intrinsic faintness of the sources in this band, none of the targets were detected by UVOT.

The *Swift*-XRT observations were executed in the photon counting mode. The XRT data were analysed with the XRTDAS software package (v.3.0.0) distributed by HEASARC within the HEASoft package (v.6.17). We used the task *xrtpipeline* to calibrate and clean the event files. Using the tool XSELECT, we extracted the source and background regions using circles and annuli centered on the source, respectively. The radii for the two regions were chosen taking into account the difference in count rates for the three objects. For 3FGL J0325.5+2223 we used a circular region of 45″radius, and an annular region of inner radius 90″and outer radius 190″; for 3FGL J0449.0+1121 we used a circular region of 12″radius, and an annular region of

inner radius 40″and outer radius 140″; and for 3FGL J0453.2−2808 we used a circular region of 25″radius, and an annular region of inner radius 50″and outer radius 150″.
The ancillary response files were generated using *xrtmkarf* and the source spectra were rebinned to have at least one count per bin.

3.1.4 GROND

GROND is a multi-channel imager mounted on the 2.2 m MPG[4] telescope at ESO in La Silla, Chile. It simultaneously observes with seven filters (g', r', i', z', *J, H,* K_s), covering the optical to near-infrared wavelength regime (Greiner et al., 2008). The data analysis procedure is described in detail in Krühler et al. (2008). For the optical filters (g', r', i', z'), the point spread function (PSF) photometric technique was employed, whereas the aperture extraction method was applied for the near-infrared (*J, H,* K_s) filters, because of the undersampled PSF in these bands. The optical filters were calibrated with the SDSS Data Release 8 (Aihara et al., 2011) and the near-IR filters were calibrated with 2MASS stars (Skrutskie et al., 2006). We have corrected for Galactic extinction following Schlafly & Finkbeiner (2011). The resulting magnitudes were converted to the AB magnitude system and are provided in Table 3.1.

3.2 Results

3.2.1 X-ray Spectral analysis

The joint *Swift*-XRT (0.3-10 keV) and *NuSTAR* (3.0-79 keV) spectra were simultaneously fitted with XSPEC using the C statistic (Cash, 1979). For all three sources we included Galactic absorption ($N_{\rm H}$) with Galactic neutral hydrogen column densities taken from Kalberla et al. (2005).

A power-law model with absorption fixed at the Galactic value was used in all three cases. We included a multiplicative constant factor to cross-calibrate the three instruments; we kept it equal to 1 for FPMB but left it free to vary for FPMA and *Swift*-XRT. For two of the targets, the difference for FPMA is in the range of 6-7 %, while for *Swift*-XRT it is in the 3-20 % range. This is consistent with what has already been found for

[4]https://www.eso.org/sci/facilities/lasilla/telescopes/national/2p2.html

other sources (e.g., Madsen et al., 2015). In the case of 3FGL J0449.0+1121, due to poor photon statistics, we decided to keep the cross-calibration constant fixed to 1 for both FPMA and FPMB. Within errors, the cross-normalization constant for *Swift*-XRT is compatible with 1. The results of the spectral fits are provided in Table 3.1 and Figure 3.1 shows the combined spectrum for the three sources.

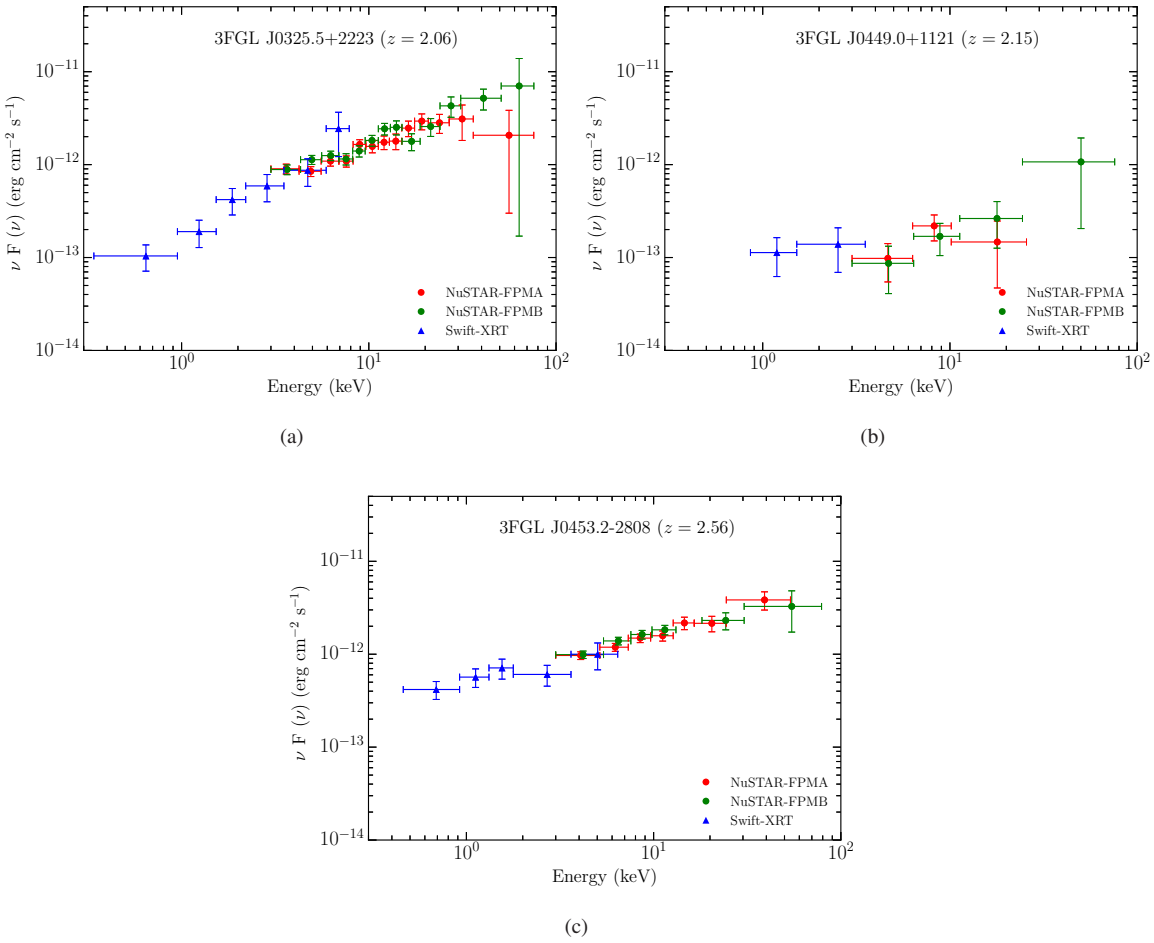

Figure 3.1: Combined *Swift*-XRT and *NuSTAR* (FPMA and FPMB) observations of 3FGLJ0325.5+2223 on 2015 November 11, 3FGLJ04490+1121 on 2015 December 2, and 3FGLJ04532-2808 on 2015 December 3.

3.2.2 SED modeling

To understand the underlying physical mechanisms powering the relativistic jets of these objects, we reproduced the broadband SEDs using a simple one zone leptonic emission model. The details of the adopted procedure can be found in Ghisellini & Tavecchio (2009) and here it is briefly described. The observed radi-

Table 3.1: Table of Observations and Spectral Parameters

Fermi-LAT								
Name	Time Covered	Flux[a]	Photon Index[b]	Test Statistic[c]				
3FGL J0325.5+2223	2015-03-01−2016-03-01	5.57 ± 1.12	2.37 ± 0.09	76.36				
3FGL J0449.0+1121	2015-03-01−2016-03-01	11.90 ± 1.50	2.35 ± 0.06	229.62				
3FGL J0453.2−2808	2015-03-01−2016-03-01	8.11 ± 1.22	2.49 ± 0.08	195.91				
NuSTAR + *Swift*-XRT								
Name	Date	$N_{\rm H}$ [d]	Photon Index [e]	Flux [f]	C-Stat/dof			
3FGL J0325.5+2223	2015-11-08	8.92	$1.36^{+0.10}_{-0.09}$	$7.44^{+0.81}_{-1.13}$	643.74/823			
3FGL J0449.0+1121	2015-12-02	12.6	$1.46^{+0.44}_{-0.43}$	$1.05^{+0.40}_{-0.91}$	291.47/331			
3FGL J0453.2−2808	2015-12-03	2.05	1.52 ± 0.10	$6.64^{+0.91}_{-0.70}$	625.66/769			
GROND								
Name	UT Date[g]	AB Magnitude[h]						
		g'	r'	i'	z'	J	H	K_s
3FGL J0325.5+2223	2015-11-15.49	18.91 ± 0.05	18.78 ± 0.04	18.58 ± 0.05	18.25 ± 0.05	18.36 ± 0.11	18.40 ± 0.13	17.91 ± 0.16
3FGL J0449.0+1121	2015-12-08.31	21.17 ± 0.05	18.49 ± 0.05	18.49 ± 0.04	18.32 ± 0.05	17.94 ± 0.12	17.50 ± 0.14	17.05 ± 0.14
3FGL J0453.2−2808	2016-06-01.63	17.35 ± 0.29	17.42 ± 0.30	17.49 ± 0.29	17.37 ± 0.28	16.96 ± 0.10	16.72 ± 0.12	16.49 ± 0.13

Notes:

[a] Integrated γ-ray flux in the $0.06 - 300$ GeV energy range in units of 10^{-8} photons $\rm cm^{-2}\,s^{-1}$.

[b] Photon index calculated from γ-ray analysis.

[c] Test statistic is a measure of significance of detection ($\sigma \sim \sqrt{\rm TS}$; Mattox et al., 1996).

[d] Column density in units of 10^{20} $\rm cm^{-2}$.

[e] Photon index calculated from X-ray analysis.

[f] Observed flux in units of 10^{-12} erg $\rm cm^{-2}\,s^{-1}$ in the $0.3 - 79$ keV energy band. The errors are at the 90% level of confidence for one parameter of interest and the fluxes are corrected for the Galactic absorption.

[g] Exposure start time.

[h] Corrected for Galactic reddening.

ation was assumed to originate from a spherical emission region covering the entire cross-section of the jet, located at a distance of $R_{\rm diss}$ from the central engine, and moving with the bulk Lorentz factor Γ. The jet semi opening angle was assumed to be 0.1 rad. The relativistic electron population was assumed to follow a broken power law energy distribution of the following type

$$N(\gamma) \propto \frac{(\gamma_{\rm break})^{-p}}{(\gamma/\gamma_{\rm break})^{p} + (\gamma/\gamma_{\rm break})^{q}}. \tag{3.1}$$

where $\gamma_{\rm break}$ is the break energy, p and q are the slopes of the particle energy distribution before and after $\gamma_{\rm break}$, respectively. In the presence of a tangled but uniform magnetic field B, electrons radiate via synchrotron and IC mechanisms. For the IC process, the low energy photons considered are synchrotron photons and photons originating outside the jet. We have considered several AGN components as potential reservoirs of external radiation energy density: (a) the accretion disk emission; (b) the X-ray corona lying above and below the accretion disk, having a cut-off power law spectral shape, and reprocessing 30% of the disk luminosity ($L_{\rm disk}$); (c) the broad line region (BLR); and (d) the dusty torus. Both the BLR and the torus are considered as spherical shells located at distances $R_{\rm BLR} = 10^{17} L_{\rm disk,45}^{1/2}$ cm and $R_{\rm IR} = 10^{18} L_{\rm disk,45}^{1/2}$ cm, respectively, where $L_{\rm disk,45}$ is the accretion disk luminosity in units of 10^{45} erg $\rm s^{-1}$. They are assumed to re-emit 10% and 50% of $L_{\rm disk}$ and their spectral shapes are considered as a blackbody peaking at the Lyman-

Table 3.2: Summary of the parameters used/derived from the SED modeling of three MeV blazars shown in Figure 3.2. A viewing angle of 3° is adopted for all of them.

Parameter	J0325.5+2223	J0449.0+1121	J0453.2−2808
Slope of the particle distribution below the break energy (p)	1.45	1.55	1.95
Slope of the particle distribution above the break energy (q)	3.9	4.15	4.1
Magnetic field in Gauss (B)	3.2	1.5	2.5
Particle energy density in erg cm^{-3} (U_e)	0.03	0.01	0.01
Bulk Lorentz factor (Γ)	10	12	10
Minimum Lorentz factor ($\gamma_{\rm min}$)	1	6	1
Break Lorentz factor ($\gamma_{\rm break}$)	57	310	139
Maximum Lorentz factor ($\gamma_{\rm max}$)	3e3	3e3	3e3
Dissipation distance in parsec ($R_{\rm Sch}$)	0.18 (3090)	0.23 (4850)	0.37 (3900)
Size of the BLR in parsec (in $R_{\rm Sch}$)	0.18 (3091)	0.19 (4006)	0.35 (3709)
Black hole mass in log scale, in units of solar mass ($M_{\rm BH,m}$)	8.8	8.7	9.0
Accretion disk luminosity in log scale ($L_{\rm disk}$, erg s^{-1})	46.48	46.54	47.08
Accretion disk luminosity in Eddington units ($L_{\rm disk}/L_{\rm Edd}$)	0.40	0.56	0.95
Characteristic temperature of IR-torus in Kelvin ($T_{\rm IR}$)	500	500	500
Observed variability time scale in days ($t_{\rm var}$)	4	5	10
Jet power in electrons in log scale ($P_{\rm e}$, erg s^{-1})	44.87	44.52	44.90
Jet power in magnetic field in log scale ($P_{\rm B}$), erg s^{-1}	46.06	45.79	46.49
Radiative jet power in log scale ($P_{\rm r}$, erg s^{-1})	45.74	45.60	45.92
Jet power in protons in log scale ($P_{\rm p}$, erg s^{-1})	47.18	46.15	47.43

alpha frequency and $T_{\rm IR}$, respectively, where $T_{\rm IR}$ is the characteristic temperature of the torus. The EC spectra were calculated by deriving the comoving frame radiative energy densities from these components. Finally, we evaluated various powers that the jet carries in the form of the magnetic field ($P_{\rm m}$), electrons ($P_{\rm e}$), radiation ($P_{\rm r}$), and protons ($P_{\rm p}$). The $P_{\rm p}$ or kinetic jet power was estimated by considering protons to be cold and hence contributing only to the inertia of the jet and having an equal number density to that of relativistic electrons (e.g., Celotti & Ghisellini, 2008).

The parameters associated with the SED modeling are given in Table 3.2 and the results are plotted in Figure 3.2.

3.2.3 Black hole mass estimation

The most commonly used approach to calculate quasar black hole mass is adopting a single epoch optical spectroscopic measurement, which assumes that the BLR is virialized (e.g., Shen et al., 2011). Another novel method to derive the black hole mass is by reproducing the IR-UV spectra of quasars with a standard Shakura & Sunyaev (1973) accretion disk, provided the big blue bump is visible in this energy band (see, Ghisellini & Tavecchio, 2015). This is particularly useful when the optical/IR spectrum of the source is not

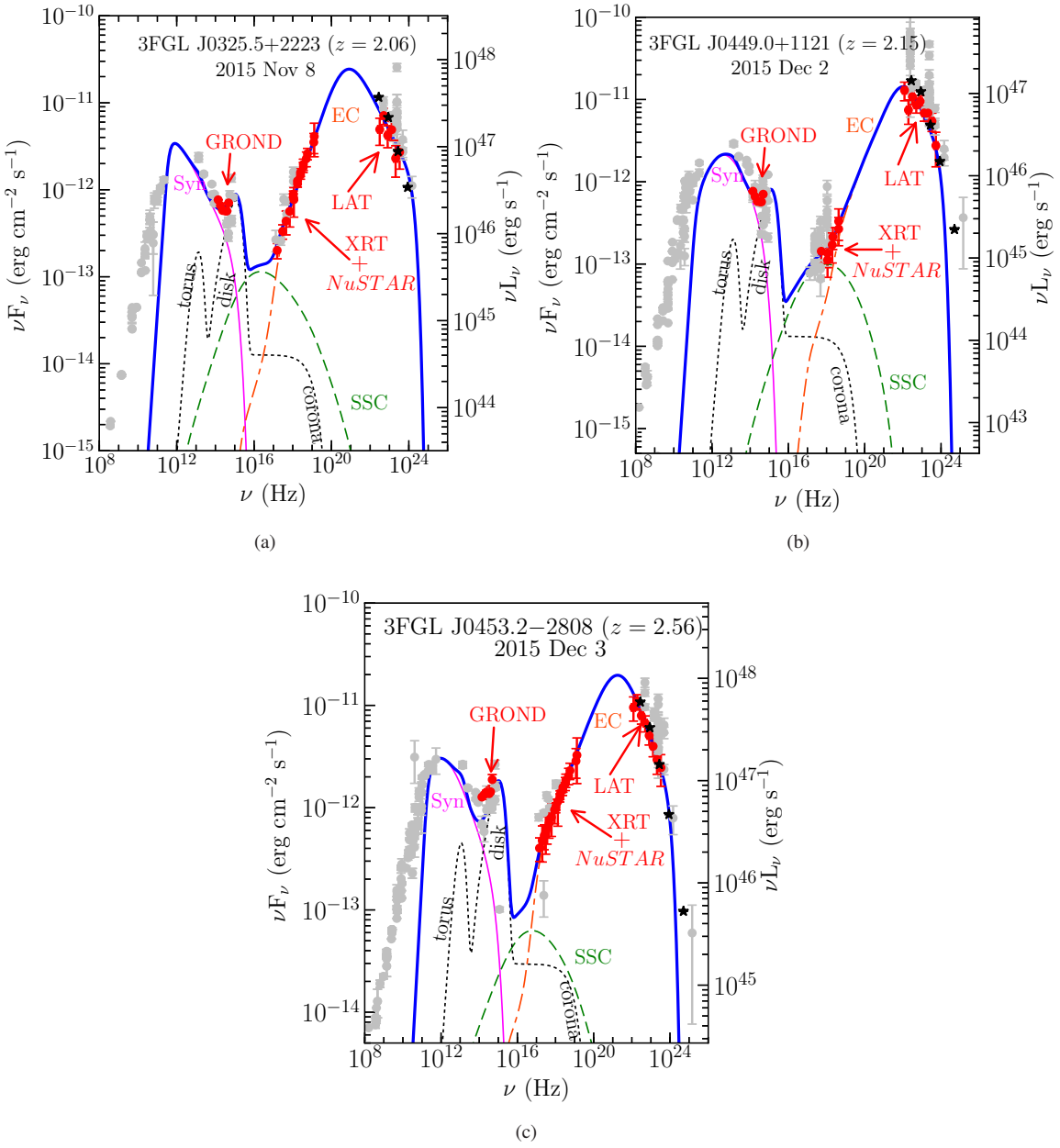

Figure 3.2: The broadband SED of three quasars using quasi-simultaneous GROND, *Swift*, *NuSTAR*, and *Fermi*-LAT data, modeled using the one zone leptonic emission model described in the text. Grey and red circles represent the archival and quasi-simultaneous observations, respectively. In the *Fermi*-LAT energy range, black stars denote the 3FGL spectrum.

available. In this technique, the spectral shape of the accretion disk is assumed as a multi-color blackbody

with the following flux density profile (Frank et al., 2002)

$$F_\nu = \nu^3 \frac{4\pi h \cos\theta_{\rm v}}{c^2 D^2} \int_{R_{\rm in}}^{R_{\rm out}} \frac{R\,{\rm d}R}{e^{h\nu/kT(R)} - 1}, \tag{3.2}$$

where D is the distance of the observer, k is the Boltzmann constant, c is the speed of light, and $R_{\rm in}$ and $R_{\rm out}$ are the inner and outer disk radii, taken as $3R_{\rm Sch}$ and $500R_{\rm Sch}$, respectively. $R_{\rm Sch}$ is the Schwarzschild radius. The radial temperature profile can be given as

$$T(R) \,=\, \frac{3R_{\rm Sch}L_{\rm disk}}{16\pi\eta_{\rm a}\sigma_{\rm SB}R^3}\left[1-\left(\frac{3R_{\rm Sch}}{R}\right)^{1/2}\right]^{1/4}, \tag{3.3}$$

where $\sigma_{\rm SB}$ is the Stefan-Boltzmann constant and $\eta_{\rm a}$ is the accretion efficiency, adopted here as 10%. There are only two parameters, the black hole mass and the accretion rate $\dot{M}_{\rm a}$, to determine. The rate of accretion can be computed from the intrinsic accretion disk luminosity $L_{\rm disk} = \eta_{\rm a}\dot{M}_{\rm a}c^2$. Since $L_{\rm disk}$ can be obtained from observations, provided the peak of the big blue bump is visible in the SED, this leaves only the black hole mass as a free parameter (e.g., Ghisellini & Tavecchio, 2015).

The black hole masses of two out of three sources, 3FGL J0325.5+2223 and 3FGL J0449.0+1121, were derived by Shaw et al. (2012) using the optical spectroscopic approach. Using the C IV line, they found masses of $1.6\times10^9\ M_\odot$ and $7.9\times10^7\ M_\odot$ for 3FGL J0325.5+2223 and 3FGL J0449.0+1121, respectively. For 3FGL J0453.2−2808, we used C IV line parameters from Fricke et al. (1983) and adopted the empirical relations of Shen et al. (2011) to derive a central black hole mass of $\sim 7.9\times10^8\ M_\odot$. Instead following the SED modeling approach, we found black hole masses for 3FGL J0325.5+2223, 3FGL J0449.0+1121 and 3FGL J0453.2−2808 of 6.3×10^8, 5.0×10^8 and $1.0\times10^9\ \ M_\odot$, respectively (all black-hole masses are listed in Table 3.3). The black hole masses computed from both approaches reasonably match within a factor of 2 for two of the sources[5], though the SED modeling predicts a higher black hole mass (factor of ∼6) for 3FGL J0449.0+1121.

[5]It should be noted that the typical errors in virial spectroscopic black hole mass calculation is ∼0.4 dex (e.g., Shen et al., 2011; Vestergaard & Peterson, 2006)

Table 3.3: Table of Black-Hole Masses, derived both from spectroscopic approach and SED modelling.

	3FGL J0325.5+2223	3FGL J0449.0+1121	3FGL J0453.2−2808
$M_{\rm BH,SED}$ ($M_\odot$)	6.3×10^8	5.0×10^8	1.0×10^9
$M_{\rm BH,spectroscopy}$ ($M_\odot$)	1.6×10^9	7.9×10^7	7.9×10^8

3.3 Discussion

High-redshift blazars are bright targets in hard X-rays. This is probably due to the shift of blazar SED towards longer wavelengths as their non-thermal luminosity increases (Fossati et al., 1999). The shifting causes their spectra to become steeper at γ-rays ($\Gamma_\gamma \gtrsim 2.3$) and harder at X-rays ($\Gamma_{\rm X} \lesssim 1.5$). Indeed, all the three MeV blazars studied here display these features (see Table 3.1). In this regard, observations in both these energy bands are crucial to determine the power of the jet and explore its connection to accretion. In fact, having both *NuSTAR* and *Fermi*-LAT detections for all three sources provides a unique opportunity to locate the IC peak and study the shape of the underlying electron population. The bolometric emission in such powerful blazars is dominated by high energy X-ray and γ-rays radiation conveying that good quality spectral measurements in both bands are desirable. Furthermore, there are a few other interesting properties of high redshift blazars revealed by *NuSTAR* monitoring. This includes a spectral flattening seen in the joint *Swift*-XRT and *NuSTAR* spectrum of various MeV blazars (Paliya et al., 2016) and also a substantial flux variability seen at two different epochs of *NuSTAR* monitoring (e.g., Tagliaferri et al., 2015). The latter becomes more important due to the fact that these sources are weaker at γ-rays and may not have enough signal to detect significant variability in this energy range. As a result, *NuSTAR* has proved to be a fundamental instrument to pursue high-redshift blazar studies.

The joint XRT and NuSTAR spectra of the three sources do not show any curvature within the available statistics and is well fitted by a simple absorbed power law model with $N_{\rm H}$ fixed to the Galactic value. It is reported in various recent studies that the 0.3-79 keV X-ray spectra of many MeV blazars (> 5) show a distinct curvature or a break around $\sim$few keV (e.g. Paliya et al., 2016; Tagliaferri et al., 2015). Such a feature reflects the behavior of the emitting electron distribution, intrinsic to the jet, rather than any other external factors (Paliya et al., 2016, and references therein). On the other hand, there are observations of MeV blazars, that do not show any such feature (e.g. Ajello et al., 2016). In fact, the shape of the X-ray spectrum constrains the behavior of the underlying electron population, especially the low energy cut-off of the electrons ($\gamma_{\rm min}$) provided the X-ray emission is dominated by EC process, rather than by SSC (see, e.g.,

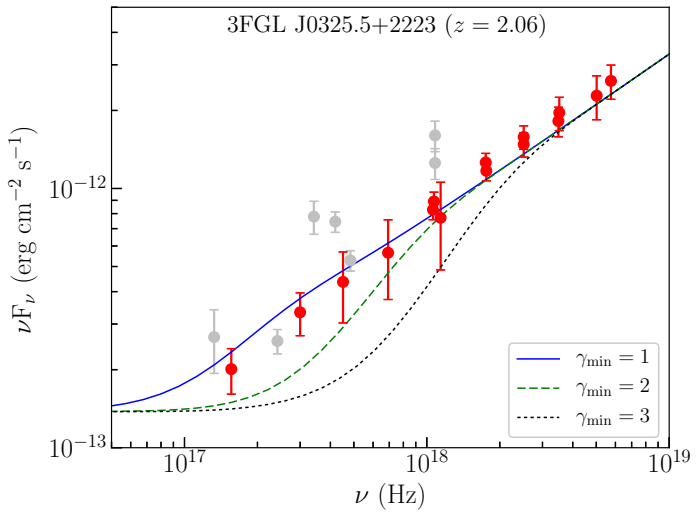

Figure 3.3: Zoomed SED of 3FGL J0325.5+2223, showing the X-ray spectrum. The different lines represent the modeling done with various $\gamma_{\rm min}$ values (as labelled). As can be seen, in this source the low-energy cut-off cannot be significantly larger than unity.

Celotti & Ghisellini, 2008). This is illustrated in Figure 3.3. As can be seen, a good fit can be achieved only with $\gamma_{\rm min} \sim 1$. For higher values, the model predicts a significant break in the X-ray spectrum, which is not seen[6]. This implies the joint XRT and *NuSTAR* observations are instrumental in evaluating the minimum energy of the underlying particle population, which ultimately controls the jet power.

The broadband SEDs of the three MeV sources resemble those of powerful blazars. The synchrotron peaks lie in the sub-mm range, whereas the high-energy IC peaks lie in the MeV band. The Compton dominance (the ratio of IC to synchrotron peak luminosities) is found to be >1 for all three blazars. The GROND observations reveal a break in the IR-optical spectra of the sources which we interpret as a combination of the falling synchrotron spectrum and the rising accretion disk radiation. Though we do not see the peak of the disk emission (primarily due to lack of UV data), based on the shape of the GROND spectra and the available archival broad line luminosities (Fricke et al., 1983; Shaw et al., 2012), we are able to derive both the disk luminosity and the central black hole mass. Another constraint is provided by the broader limiting range of the disk luminosity that can be set by considering $10^{-2} L_{\rm Edd} < L_{\rm disk} < L_{\rm Edd}$. The upper limit ensures the source to be sub-Eddington and the lower limit assumes the accretion disk is radiatively efficient. Furthermore, combining the observations from *Swift*-XRT, *NuSTAR* and *Fermi*, we can cover the X- and

[6]We caution that our calculations at low values of γ are rather approximate. These relatively 'cold' electrons could be involved in bulk Compton process (Celotti et al., 2007) and one should self-consistently take this into account. However, this feature is yet to be observed (however see, Ackermann et al., 2012, for a possible detection) and so its contribution is uncertain. Furthermore, the kinetic jet power is very sensitive to $\gamma_{\rm min}$ and for $\gamma_{\rm min} \gg 1$ it falls below the jet power in radiation, which is problematic for powerful FSRQs (see, e.g. Ghisellini et al., 2014)

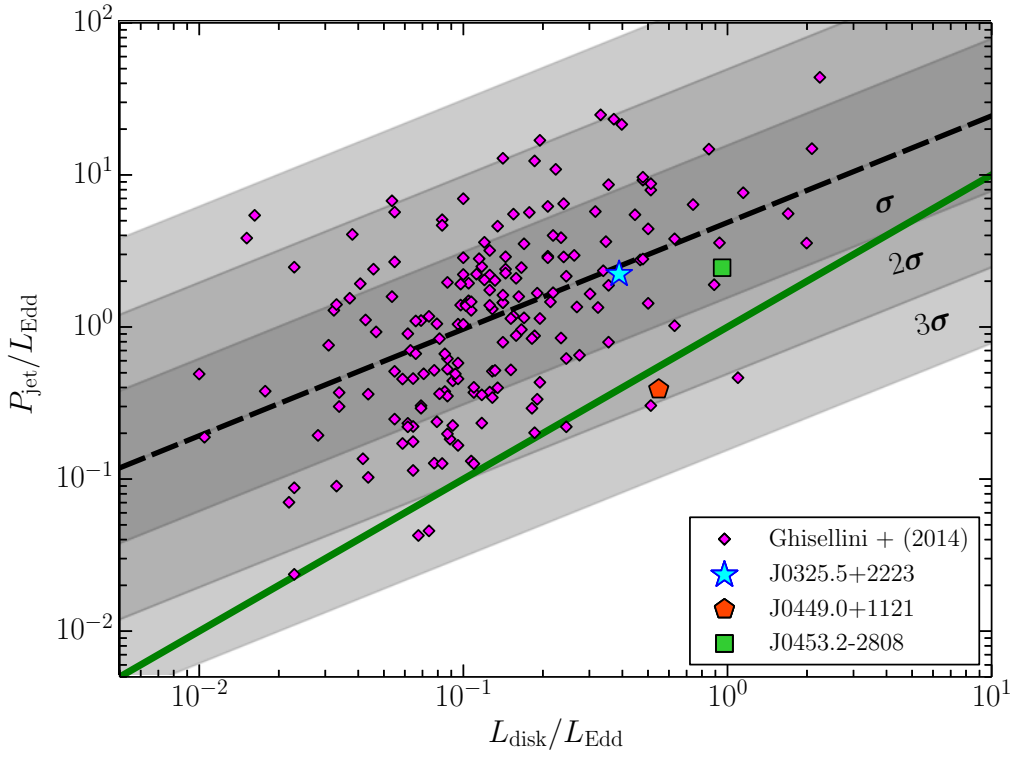

Figure 3.4: Comparison of jet powers and accretion disk luminosities of three MeV sources with that of a large sample of blazars studied by Ghisellini et al. (2014). Black dashed and green solid lines represent the best fit and one-to-one correlation of the plotted quantities, respectively. Both jet powers and disk luminosities are normalized for central black hole mass.

γ-ray portions of the spectrum. These parts of the SEDs are successfully reproduced by IC scattering of low energy photons produced externally to the jet.

Since in the adopted model the radiative energy densities of various AGN components are functions of the distance from the central engine, we are able to determine the location of the emission region. This is found to be at the outer edge of the BLR where a major fraction of the seed photons are supplied by the BLR clouds. The X-ray spectra of all three objects are extremely hard and observations further hint at the dominance of the EC process over SSC emission in this energy range (see, Ajello et al., 2016, for a detailed discussion). On the other hand, the γ-ray SEDs are steep, as expected in high redshift blazars. The spectral shapes observed at X-ray and γ-ray energies help constrain the slopes of the underlying broken power law electron energy distribution. Overall, the observed SED parameters of these three sources are similar to other high-redshift MeV blazars (e.g., Ghisellini et al., 2010).

With good quality IR-optical (constraining the accretion disk emission) and hard X-ray-γ-ray data (required for the accurate measurement of the jet power) in hand, it is interesting to compare the disk-jet connection observed in the three MeV blazars studied in this work with that for other blazars. With this in mind, we collect the jet powers and disk luminosities of all blazars studied by Ghisellini et al. (2014). In Figure 3.4, we plot the jet power as a function of the disk luminosity for blazars, including our three MeV sources. The plotted quantities are normalized for the central black hole mass. As can be seen, the majority of sources have normalized jet power exceeding their normalized disk luminosities (the one-to-one correlation is shown by the green solid line). 3FGL J0325.5+2223 and 3FGL J0453.2−2808 have their jet powers larger than their disk luminosities, though 3FGL J0449.0+1121 lies just below the one-to-one correlation. Indeed, among the three objects, this object has the least jet power. The jet powers of both 3FGL J0325.5+2223 and 3FGL J0453.2−2808 appear to be larger than the Eddington luminosity ($P_{\rm jet}/L_{\rm Edd} > 1$). However, there are a few caveats. The existence of electron-positron pairs in the jet would reduce the jet power by $n_{\rm e}/n_{\rm p}$ (where $n_{\rm e} \equiv n_{e^-} + n_{e^+}$, see, Pjanka et al., 2017, for a detailed discussion), although their number could not greatly exceed the protons in order to avoid the Compton rocket effect that would otherwise stop the jet (Ghisellini & Tavecchio, 2010). Furthermore, the budget of the jet power can also come down if one considers a spine-sheath structured jet, instead of a one-zone uniform emission region (Sikora et al., 2016). Most importantly, the underestimation of the black hole mass can also lead to super-Eddington jet power. Consequently, one has to take into account these uncertainties and/or their combination before drawing any firm conclusion.

Chapter 4

Conclusions and Outlook

4.1 Conclusions

MeV blazars are some of the most extreme sources in the Universe. With bolometric luminosities exceeding 10^{48} erg s^1 and powerful relativistic jets ($P_j \geq \dot{M}c^2$), they are detected at high-redshifts ($z > 2$) and they generally harbor extremely massive black holes ($M_{BH} \sim 10^9 M_\odot$). Measurements of their physical properties (bolometric, jet and accretion luminosity, Γ, angle of the jet and black hole mass) are fundamental paramenters to understand this source class and use them to probe the formation of massive black holes in the early Universe.

In this work we studied three high redshift ($z > 2$) MeV blazars using quasi-simultaneous GROND, *Swift*, *NuSTAR*, and *Fermi*-LAT data, focusing on the hard X-ray part uncovered by *NuSTAR*. With the latter and the aid of the *Fermi*-LAT data we were able to constrain the position of the IC peak and to derive related characteristics of these sources like bolometric luminosity, jet power as well as the relativistic particle distribution and the location of the emission region. Our primary findings are as follows

1. All sources are significantly detected by *NuSTAR* and exhibit a flat (photon index $\lesssim 1.5$) X-ray spectrum extended up to 79 keV, as revealed from joint XRT and *NuSTAR* fitting.

2. The broadband SEDs of these sources resembles that of powerful blazars with synchrotron and IC

peaks lying at sub-mm and MeV energy ranges, respectively.

3. The IR-optical spectra can be explained by a combination of synchrotron and accretion disk spectrum, whereas, high energy X-ray to γ-ray radiation is successfully reproduced by IC scattering of low energy photons mainly supplied by the BLR.

4. The location of the emission region is found to be at the outer edge of the BLR in all three sources. The black hole masses for all three sources are greater than $10^{8.6}\ M_{\odot}$.

5. Comparing the normalized jet powers and disk luminosities of these sources with that of a large sample of blazars, we find them to lie on the well known disk-jet correlation derived by Ghisellini et al. (2014) where their jet powers exceed accretion disk luminosities. Only 3FGL J0449.0+1121 shows a slight offset from this correlation.

4.2 Outlook

With the launch of *NuSTAR*, the study of high-redshift blazar has seen an major improvement. Being able to cover the hard X-ray band with unprecedent detail has been fundamental to place more accurate constraints on the high-energy part of blazars' SED and on the location of the IC peak, hence on the measurements

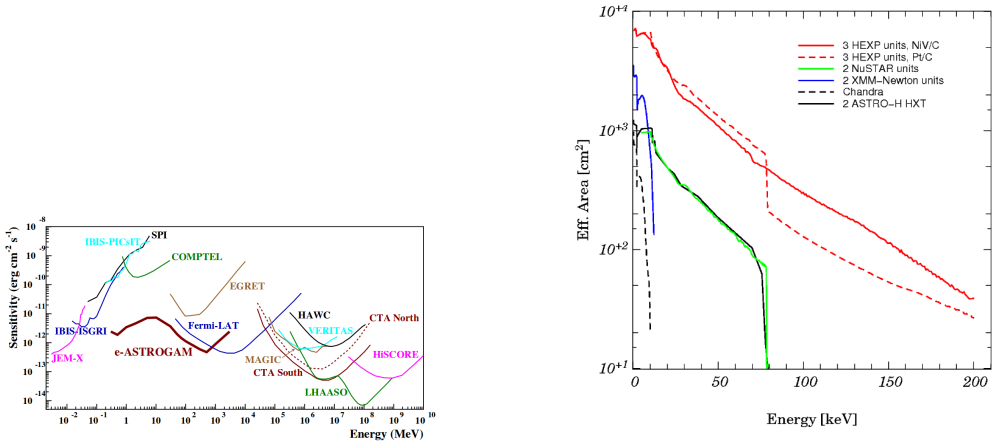

(a) (b)

Figure 4.1: Left panel(a): point source continuum sensitivity of different X- and -ray instruments (De Angelis et al., 2016). Right panel(b): effective area vs. energy for HEX-P and current/near-term focusing missions (Harrison & HEX-P Collaboration Collaboration, 2017).

of the jet power. However, the pointing strategy of *NuSTAR* allows us to monitor only a few objects and an energy gap, from the hard X-rays and the γ-rays, still remains uncovered. The preferred instrument would be an all-sky survey MeV telescope, such as e-ASTROGAM or HEX-P (see, De Angelis et al., 2016; Harrison & HEX-P Collaboration Collaboration, 2017). Those are still probe missions that, if accepted, would be in orbit in a few years.

On the other hand, we could use the capabilities of the *Fermi*-LAT. *Fermi* has completed eight years of continuous sky monitoring, implying a lower flux threshold, thus a higher probability of detecting faint objects. Also, the recently released Pass 8 dataset has a better sensitivity at lower frequencies ($<$200 MeV), crucial for high-z blazars. As of now, the maximum energy range used in *Fermi*-LAT data analysis is 60 MeV to 300 GeV (Ackermann et al., 2017). The idea would be to perform all-sky simulations to understand if it is possible to lower even more the energy threshold of the LAT. This would allow us to use the full energy band covered by the instrument (20 MeV-300 GeV) and to cover a fundamental part of the spectrum of high-z blazars.

Appendices

Appendix A Relativistic Beaming

According to special relativity, space and time differ as seen in two different reference frames. The basic Lorentz transformation, for a comoving frame K' and a stationary frame K (assuming motion only in the x-axis), are:

$$\begin{aligned} x' &= \gamma(x - vt) \\ y' &= y \\ z' &= z \\ t' &= \gamma(t - \beta\frac{x}{c}) \end{aligned} \tag{1}$$

where $\beta = \frac{v}{c}$ and $\gamma = 1/(1-\beta^2)^{1/2}$ is the Lorentz factor. The length of a moving ruler measured at the same time t in the two frames is:

$$\begin{aligned} \Delta x' = x'_2 - x'_1 = \gamma(x_2 - x_1) = \gamma\Delta x \\ \Delta x = \Delta x'/\gamma \rightarrow contraction \end{aligned} \tag{2}$$

Similarly, comparing time intervals at the same position x':

$$\begin{aligned} \Delta t' = t'_2 - t'_1 = (t_2 - t_1)/\gamma = \Delta t/\gamma \\ \Delta t = \gamma\Delta t' \rightarrow dilation \end{aligned} \tag{3}$$

A.1 Time

Consider a light source moving at a velocity $v = \beta c$ at an angle θ with respect to the observer. Consider that in K' the source stays on for a time $\Delta t'_e$. If we use photons to measure this time interval (which in special relativity would be $\Delta t_e = \gamma\Delta t'_e$), we also need to take into account the fact that the first and last photon have

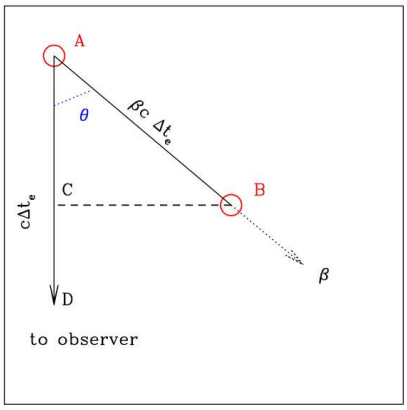

Figure 2: Schematic of a light source moving at an angle θ with respect to the observer from A to B (adapted from Ghisellini, 2013a).

been emitted at different points, hence their travel path is different. Consider Figure 2. The first photon is emitted in A and the last in B. In the frame K, the path AB is

$$AB = \beta c \Delta t_e = \gamma \beta c \Delta t'_e \tag{4}$$

While the source moved from A to B, the photon emitted at point A traveled a distance AB and is now in D ($AD = c\Delta t_e$). Along the line of sight, the first and last photon are separated by a distance CD. Therefore the time interval given by CD/c is the arrival time difference between the first and last photon ($\Delta t_a = CD/c$):

$$\begin{aligned} \Delta t_a = \frac{CD}{c} = \frac{AD - AC}{c} = \\ = \Delta t_e (1 - \beta \cos\theta) \\ = \Delta t'_e \gamma (1 - \beta \cos\theta) \\ = \frac{\Delta t'_e}{\delta} \end{aligned} \tag{5}$$

where $\delta = \frac{1}{\gamma(1-\beta\cos\theta)}$ is called the relativistic Doppler factor.

- for $\theta = 90°$, $\delta = 1/\gamma$

- for θ small, 1/(1-$\beta\cos\theta$) becomes large compensating for $1/\gamma$
- for $\cos\theta = \beta$ ($\sin\theta = 1/\gamma$), $\delta = \gamma$
- for $\theta = 0°$, $\delta = \gamma(1+\beta)$

As the frequency is an inverse of time, it will transform as

$$\nu = \nu'\delta \tag{6}$$

A.2 Aberration

When a source is moving, another important effect that comes into play is the aberration of light: two observers in different reference frames see light coming from different angles. The angle transformations between two inertial frames are:

$$\begin{aligned} \sin\theta &= \frac{\sin\theta'}{\gamma(1+\beta\cos\theta')} \qquad & \sin\theta' &= \frac{\sin\theta}{\gamma(1-\beta\cos\theta)} \\ \cos\theta &= \frac{\cos\theta'+\beta}{(1+\beta\cos\theta')} \qquad & \cos\theta' &= \frac{\cos\theta-\beta}{(1-\beta\cos\theta)} \end{aligned} \tag{7}$$

Note that if $\theta = 90°$, $\sin\theta = 1/\gamma$ and $\cos\theta = \beta$. If a source moving at relativistic speed in K' is emitting isotropically (assume it emits half of its photon is a hemisphere), in K the same source will appear to emit half of its photons in a cone of semi-aperture 1/γ. The transformation of the solid angle (assuming symmetry about ϕ) is:

$$d\Omega = 2\pi d\cos\theta = \frac{d\Omega'}{\gamma^2(1+\beta\cos\theta')^2} = \frac{d\Omega'}{\delta^2} \tag{8}$$

A.3 Intensity and Luminosity

The monochromatic intensity transforms as:

$$\begin{aligned} I(\nu) &= h\nu \frac{dN}{dt d\nu d\Omega dA} \\ &= \delta^3 I'(\nu') = \delta^3 I'(\nu/\delta) \end{aligned} \tag{9}$$

Integrating over all frequencies, we obtain the bolometric intensity which transforms as:

$$I = \delta^4 I' \tag{10}$$

If we are dealing with a single, spherical blob, the luminosity is $L = 4\pi d_L^2 F$, where F is the observed flux and d_L is the luminosity distance of the source. As $F \propto I$, then F transforms like I, and so does L:

$$L = \delta^4 L' \tag{11}$$

Note that this is the simplest assumption. In AGN's jets, the emission could come from different blobs in the jets or also from a continous distribution of particles. In these situations transformations are not as trivial.

A.4 Motion in a homogeneous radiation field

Jets in AGN generally move in an external radiation field (e.g. accretion disk, BLR, torus). What we are interested in calculating is then the energy density seen by an observer comoving with the jet plasma. Assume that the jet is moving at a $v = \beta c$, bulk Lorentz factor Γ and it is surrounded by a shell of external photons (BLR). For simplicity we can assume that these photons are produced by the surface of a sphere of radius R and the radiation is monochromatic ($\nu = \nu_0$ in K). The comoving observer in K' will see the radiation coming from a cone of semiaperture $1/\Gamma$. Photons coming from the forward direction ($\theta \sim 0°$) would be seen blue-shifted by a factor $\Gamma(1+\beta)$; photons coming from the side ($\theta \sim 90°$) will be seen in K' as coming from and angle given by $\sin\theta' = 1/\Gamma$, blue-shifted by a factor Γ. The intesity coming from each element is

boosted by

$$I' = \delta'^4 I \tag{12}$$

where $\delta' = \frac{1}{\Gamma(1-\beta\cos\theta')}$. The radiation energy density (integral over solid angle of the intensity) becomes:

$$\begin{aligned} U' &= \frac{2\pi}{c}\int_{\beta}^{1} I' d\cos\theta' \\ &= (1+\beta+\frac{\beta^2}{3})\Gamma^2 U \end{aligned} \tag{13}$$

The limits of the integral here correspond to the angles from 0° to 90°. In K', for $\beta \sim 1$, the radiation energy density is boosted by a factor (7/3)Γ^2.

A.5 Superluminal motion

Radio maps of AGN's jets taken at different times, revealed that the blobs in the jet were moving. Looking at radio maps taken at different times, it is possible to measure the angular displacement of a blob (i.e. $\Delta\theta$). Knowing the distance (d), it is possible to transform the angular in linear distance ($\Delta R = d\Delta\theta$). The velocity is obtained dividing this distance by the time between two radio maps (Δt_a):

$$v_{\rm app} = \frac{d\Delta\theta}{\Delta t_a} \tag{14}$$

In many jets this velocity turned out to be $v_{app} > c$! This effect is called superluminal motion. With reference at Figure 2, we can imagine that the position of the blob is measured first in A then in B by the two radio maps, projected in the plane of the sky. The observed displacement is:

$$CB = \beta c \Delta t_e \sin\theta \tag{15}$$

Dividing by Δt_a (Eq. 5), the apparent measured velocity is

$$v_{\rm app} = \frac{\beta c \Delta t_e \sin\theta}{\Delta t_a} \quad \rightarrow \quad \beta_{\rm app} = \frac{\beta \sin\theta}{1 - \beta\cos\theta} \tag{16}$$

Appendix B Radiative Processes

B.1 Emission from relativistic particles

To find the radiation emitted by particles moving at relativistic speeds the idea is to move to K' (instantaneous rest frame) (Rybicki & Lightman, 1986). Even though the particle is not at rest in this frame, it can be treated instantaneously as non-relativistic. The radiation emitted can be calculated using Larmor's formula. As the radiation is symmetric in K' with respect to any direction, its momentum is zero. Therefore, the energy in frame K moving at a velocity $-v$ with respect to the particle is:

$$dW = \gamma dW' \tag{17}$$

The time transforms as $dt = \gamma dt'$ (see Appendix A). The total power emitted in the two inertial reference frames is:

$$P = \frac{dW}{dt} \qquad P' = \frac{dW'}{dt'} \tag{18}$$

It is easy to see that

$$P = P' \tag{19}$$

The power emitted is a relativistic invariant quantity for a symmetric emitter. From Larmor's formula:

$$\begin{aligned} P = \frac{2q^2}{3c^3}\mathbf{a}' \cdot \mathbf{a}' = \frac{2q^2}{3c^3}(a'^2_{\parallel} + a'^2_{\perp}) = \\ = \frac{2q^2}{3c^3}\gamma^4(a^2_{\parallel} + \gamma^2 a^2_{\perp}) \end{aligned} \tag{20}$$

where we have used the fact that $a'_{\parallel} = \gamma^3 a_{\parallel}$ and $a'_{\perp} = \gamma^2 a_{\perp}$.

B.2 Synchrotron Radiation

Particles accelerated by a magnetic field (**B**) will radiate. For relativistic particles this radiation is known as *synchrotron* radiation. In the absence of an electric field, a particle with charge q and mass m, having a velocity **v** interacting with a magnetic field will be subject to the (relativistic) Lorentz Force.

$$\begin{aligned} \frac{d}{dt}(\gamma m\mathbf{v}) &= \frac{e}{c}\mathbf{v}\times\mathbf{B} \\ \frac{d}{dt}(\gamma mc^2) &= q\mathbf{v}\cdot\mathbf{E} = 0 \end{aligned} \tag{21}$$

Separating the parallel and perperndicular components of the velocity:

$$\frac{d}{dt}(\mathbf{v}_\parallel) = 0 \qquad \frac{d}{dt}(\mathbf{v}_\perp) = \frac{q}{\gamma mc}\mathbf{v}_\perp\times\mathbf{B} \tag{22}$$

The parallel velocity is constant and as the total $|\mathbf{v}|$=constant, also $|\mathbf{v}_\perp|$=constant. Therefore the motion of a particle in a magnetic field is described by the combination of a uniform circular motion and a uniform motion along the field which results as a helical motion. The frequency of the rotation is

$$\nu_B = \frac{qB}{\gamma mc} \tag{23}$$

The acceleration is perpendicular to the velocity and has a magnitude $a_\parallel = \nu_B v_\parallel$. The total emitted radiation is given by Larmor's formula:

$$\begin{aligned} P &= \frac{2q^2}{3c^3}\gamma^4\frac{q^2B^2}{\gamma^2m^2c^2}v_\parallel^2 = \\ &= \frac{2}{3}r_0^2c\beta_\parallel^2\gamma^2B^2 \end{aligned} \tag{24}$$

For an isotropic velocity distribution, it is necessary to average over all angles for a given speed β. The total

emitted power becomes:

$$\langle P \rangle = \frac{4}{3}\sigma_T c \beta^2 \gamma^2 U_B \tag{25}$$

where $\sigma_T = 8\pi r_0^2/3$ is the Thomson cross section (r_0 is the classical radius of an electron) and $U_B = B^2/8\pi$ is the magnetic field energy density.

The synchrotron process has an associated characteristic frequency. When the particle is relativistic, this does not correspond to the revolution period of the particle, but to the fraction of time during which, for each orbit, the observer receives some radiation. In Figure 3 the different emission radiation patterns are showed, from a non-relativistic to a relativistic regime and acceleration parallel or perpendicular to the velocity.

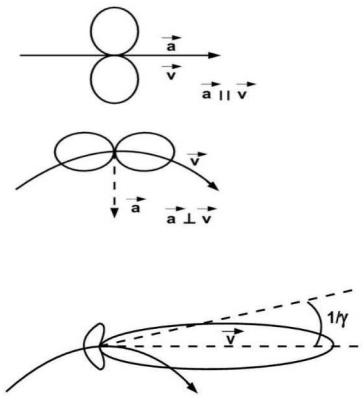

Figure 3: Radiation patterns for: (top) a non relativistic particle with the velocity parallel to the acceleration; (middle) a non relativistic particle with the velocity perpendicular to the acceleration; (bottom) relativistic particle with the velocity perpendicular to the acceleration. For a relativistic particle, the pattern strongly changes due to the aberration of light, and is strongly beamed in the forward direction (adapted from Ghisellini, 2013a).

For a relativistic particle, the radiation is strongly beamed in the forward direction in a cone of semi-aperture $1/\gamma$. To calculate the frequency at which the most power is emitted, we invert the typical timescale during which we receive the most of the signal. This time is given by

$$\Delta t_e \sim \frac{1}{\pi}\frac{1}{\gamma \nu_B} \tag{26}$$

This is the emitting time, i.e. when the electron emits radiation that will reach the observer. The measure

arrival time will be shorter (as discussed in Appendix A):

$$\Delta t_A = \Delta t_e (1-\beta) \sim \frac{1}{2\pi\gamma^3 \nu_B} \tag{27}$$

The typical synchrotron frequency is given by the inverse of this time:

$$\nu_S = \frac{1}{2\pi\Delta t_A} = \gamma^3 \nu_B = \gamma^2 \frac{eB}{2\pi m_e c} \tag{28}$$

The power per unit frequency emitted by an electron of given Lorentz factor and given pitch angle, integrated over the emission pattern, is:

$$\begin{aligned} P_S(\nu,\gamma,\theta) &= \frac{\sqrt{3}e^3 B\sin\theta}{m_e c^2} F(\nu/\nu_C) \\ F(\nu/\nu_C) &\equiv \frac{\nu}{\nu_C}\int_{\nu/\nu_C}^{\infty} K_{5/3}(y)dy \\ \nu_C &\equiv \frac{3}{2}\nu_S \sin\theta \end{aligned} \tag{29}$$

Where $K_{5/3}$ is the modified Bessel function of order 5/3. Figure 4 shows the spectrum of a single particle emission. At low frequencies, the spectrum can be approximated by a power law with slope 1/3, while at high frequencies the spectrum exponentially decays.

$$\begin{aligned} F(\nu/\nu_C) &\propto \nu^{1/3} \qquad (\nu \ll \nu_C) \\ F(\nu/\nu_C) &\propto e^{-\nu/\nu_C} \qquad (\nu \gg \nu_C) \end{aligned} \tag{30}$$

For emission from many electrons, we first need to find the energy distribution of such particles. We assume a power law distribution:

$$N(\gamma) = K\gamma^{-p} \qquad \gamma_{min} < \gamma < \gamma_{max} \tag{31}$$

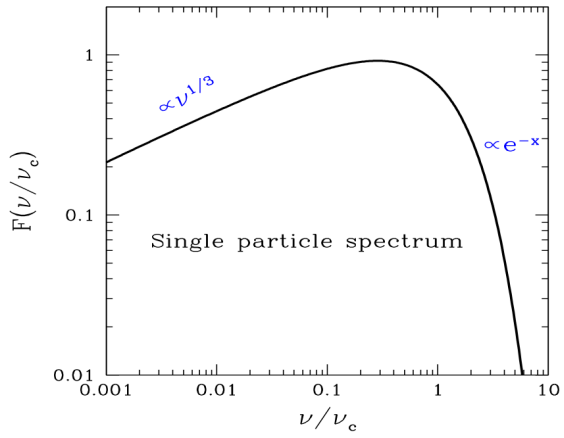

Figure 4: Synchrotron single particle spectrum (adapted from Ghisellini, 2013a).

Assuming that the pitch angle distribution is the same at low and high velocities, we want to obtain the synchrotron emissivity (power per unit solid angle produced in 1cm^3). This is:

$$\epsilon(\nu,\theta) = \frac{1}{4\pi}\int_{\gamma_{min}}^{\gamma_{max}} N(\gamma)P(\gamma,\nu,\theta)d\gamma \tag{32}$$

This integral leads to

$$\epsilon(\nu,\theta) \propto \nu^{-(p-1)/2} \tag{33}$$

A power law electron distribution produces a power law spectrum whit spectral indices correlated. Calling α the spectral index of the radiation we have:

$$\epsilon_S \propto e^{-\alpha} \qquad \alpha = \frac{p-1}{2} \tag{34}$$

The synchrotron flux received from a homogeneous thin source of volume $\propto R^3$ at a distance d_L is

$$F_S(\nu) = 4\pi\epsilon_S(\nu)\frac{V}{4\pi d_L^2} \propto \nu^{-\alpha} \tag{35}$$

All emission processes have an absorption counterpart. For synchrotron emission, we are dealing with relativistic particle that do not follow a Maxwellian distribution but rather a non-thermal one. Hence we cannot use the same arguments as for a thermal distribution to find the absorption coefficient.

Nonetheless a simplification of our problem can be to consider our distribution to be a superposition of Maxwellians of different temperatures. Then we can relate the energy $\gamma m_e c^2$ of a given electron to an energy kT of a Maxwellian. Due to the relation between absorption and emission, we can also assume that the electrons that emit some particular frequency ν can also absorb it. Therefore we can associate a 'temperature' to our frequency:

$$kT \sim \gamma m_e c^2 \sim m_e c^2 \left(\frac{\nu}{\nu_L}\right)^{1/2} \tag{36}$$

For an absorbed source we can define the brightness temperature T_b as

$$I(\nu) \equiv 2kT_b \frac{\nu^2}{c^2} \tag{37}$$

and this must be equal to the kinetic 'temperature' of the electrons:

$$I(\nu) \sim 2m_e \nu^2 \left(\frac{\nu}{\nu_L}\right)^{1/2} \propto \frac{\nu^{5/2}}{B^{1/2}} \tag{38}$$

The spectrum has become $\propto \nu^{5/2}$. Figure 5 the spectrum of a partially self absorbed source.

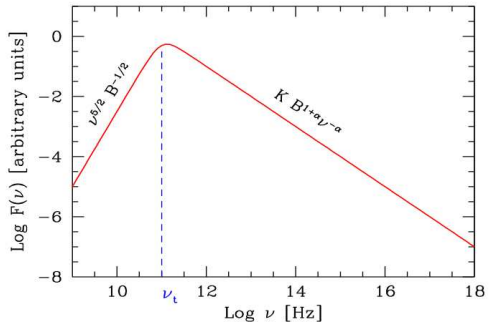

Figure 5: The synchrotron spectrum from a partially self absorbed source (adapted from Ghisellini, 2013a).

B.3 Inverse Compton Scattering

If an electron has energy higher than a typical photon energy, there can be an exchange in enegy from the electron to the photon. This process is called Compton Scattering and can happen in two regimes: Thomson, if the energy of the photon (calculated in the electron comoving frame) is less than $m_e c^2$; otherwise is Klein-Nishina. In both the typical photon gains energy even though it gets scattered at different angles.

In Figure 6, find a schematic of the inverse Compton scattering. In the frame comoving with the electron (K'), the incoming photon energy is

$$x' = x\gamma(1 - \beta\cos\psi) \tag{39}$$

where ψ is the angle between the electron velocity and the photon direction as measured in the lab frame. Considering the angle transformations listed in Appendix A, we obtain

$$x' = \frac{x}{\gamma(1 + \beta\cos\psi')} = x\delta \tag{40}$$

result that we were expecting. In the rest frame of the electron the scattered photon will have the same energy x'_1 as before the scattering, independent of the angle ($x'_1 = x'$) and will be scattered at an angle ψ'_1 with respect to the electron velocity. Going back to the lab frame

$$x_1 = x'_1\gamma(1 + \beta\cos\psi'_1) \tag{41}$$

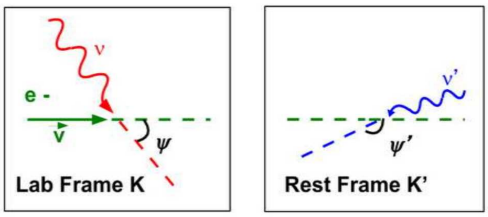

Figure 6: In the lab frame an electron is moving with velocity v that makes an angle ψ with an incoming photon of frequency ν. In the frame where the electron is at rest, the photon is coming from the front, with frequency ν' and angle ψ' with the direction of the velocity.

Rearranging for the angle transformation we get

$$x_1 = x\frac{1-\beta\cos\psi}{1-\beta\cos\psi_1} \tag{42}$$

- The maximum of energy occurs when $\psi = \pi$ and $\psi_1 = 0$, i.e. when the collision happens head-on and the photon is scattered along the electron velocity vector. In this situation

$$x_1 = 4\gamma^2 x \tag{43}$$

  where we have assumed $\gamma \gg 1$.

- On the other end the minimum energy occurs for tail-on collision ($\psi = 0$) and the photon is scattered backwards ($\psi_1 = \pi$). In this case

$$x_1 = \frac{x}{4\gamma^2} \tag{44}$$

  always assuming $\gamma \gg 1$.

- For an aperture angle of a beaming cone, $\sin\psi_1 = 1/\gamma$:

$$x_1 = \gamma^2(1-\cos\psi)x \tag{45}$$

The total energy loss rate of the electron is given by

$$P_C(\gamma) = \frac{4}{3}\sigma_T c\gamma^2\beta^2 U_r \tag{46}$$

where $U_r = \int \epsilon n(\epsilon) d\epsilon$ is the energy density radiation before scattering.

The energy loss between synchrotron and inverse Compton are very similar. In fact, if we replace the radiation energy density with the magnetic energy density, the two loss rates are the same. If relativistic electrons are in a region with both radiation and magnetic energy densities, they will emit by synchrotron as well as Inverse Compton. The ratio of the two luminosities will be

$$\frac{L_{sync}}{L_{IC}} = \frac{P_{sync}}{P_{IC}} = \frac{U_B}{U_r} \tag{47}$$

This holds true unless one of the two process is inhibited for some reason. For example, if the electron could emit and absorb synchrotron radiation, the cooling is compesated by the heating of absorption. Also, at high energies photons can scatter in the Klein-Nishina regime, where the cross section is smaller, therefore they will scatter and loose energy less.

To derive the single particle spectrum, some assumptions have to be made. The photons are assumed monochromatic, all having a dimensionless frequency $x = h\nu/m_e c^2$. In the electron rest frame, half of the photons seems to come from the front within an angle $1/\gamma$ and their typical frequency is $x' \sim \gamma x$. The scattering happens in the Thomson regime and indipendently of the incoming angle, after the interaction all the photons become isotropic. Now in the lab frame these photons have a typical frequency

$$x_1 \sim \gamma^2 x \tag{48}$$

For a monochromatic isotropic seed photons distribution, the spectrum is given by

$$\epsilon_{\rm IC} = \frac{\sigma_T n I_0 (1+\beta)}{4\gamma^2\beta^2 x_0} F_{IC}(x_1) \tag{49}$$

where $F_{\rm IC}$ contains all frequency dependences.

$$\begin{aligned} F_{\rm IC}(x_1) &= \frac{x_1}{x_0}\left[\frac{x_1}{x_0} - \frac{1}{(1+\beta)^2\gamma^2}\right] \qquad \frac{1}{(1+\beta)^2\gamma^2} < \frac{x_1}{x_0} < 1 \\ F_{\rm IC}(x_1) &= \frac{x_1}{x_0}\left[1 - \frac{x_1}{x_0}\frac{1}{(1+\beta)^2\gamma^2}\right] \qquad 1 < \frac{x_1}{x_0} < (1+\beta)^2\gamma^2 \end{aligned} \tag{50}$$

The averaged frequency of the photon spectrum is $\langle x_1 \rangle = \frac{4}{3}\gamma^2 x_0$. The emission spectrum by Inverse Compton process by electrons of different γ is shown in Figure 7.

To calculate the Inverse Compton emissivity of many electrons, we again assume a power law energy distribution (Eq. 31) and isotropic and monochromatic photons of frequency ν_0. This leads to

$$\epsilon_C(\nu_C) \propto \left(\frac{\nu_C}{\nu_0}\right)^{-\alpha} \tag{51}$$

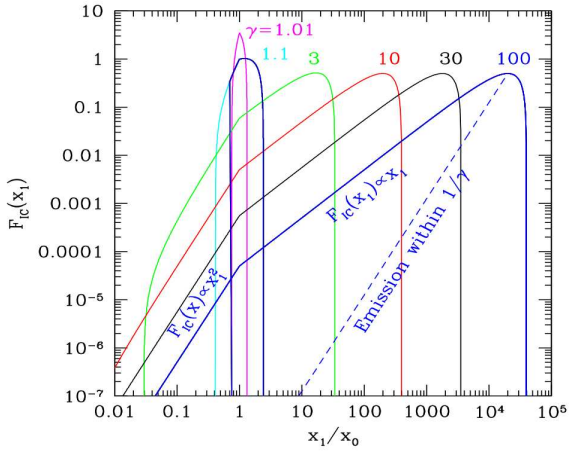

Figure 7: Spectrum emitted by the Inverse Compton process by electrons of different γ scattering an isotropic monochromatic radiation field of dimensionless frequency x_0 (adapted from Ghisellini, 2013a).

where $\alpha = \frac{p-1}{2}$. In case of non-monochromatic photons, we need to integrate over frequency range:

$$\epsilon_C(\nu_C) = \frac{1}{4}\frac{(4/3)^\alpha}{2}\frac{\tau_C}{R/c}\nu_C^{-\alpha}\int_{\nu_{min}}^{\nu_{max}}\frac{U_r(\nu)}{\nu}\nu^\alpha d\nu \tag{52}$$

B.4 Synchrotron Self Compton

Electrons in a magnetic field will radiate by synchrotron process. The photons produced will have some probability to interact with the electrons by Inverse Compton scattering. This process is called synchrotron self-Compton (SSC). Depending on the density of electrons and photons this process will be more likely to act if both are high. Now the radiation energy density is specifically the one from synchrotron:

$$U_S = 4\pi\frac{3R}{4c}\epsilon_S(\nu) \tag{53}$$

where $\frac{3R}{4c}$ is the average photon source-crossing time. The specific synchrotron emissivity can be written as

$$\epsilon_S = \epsilon_{S,0}\nu^{-\alpha} \tag{54}$$

Substituting in Equation 52:

$$\epsilon_{SSC}(\nu_C) = \frac{(4/3)^{\alpha-1}}{2}\tau_C \epsilon_{S,0} \nu_C^{-\alpha} \int_{\nu_{min}}^{\nu_{max}} \frac{d\nu}{\nu} \tag{55}$$

This integration leads to

$$\epsilon_{SSC}(\nu_C) = \frac{(4/3)^{\alpha-1}}{2}\tau_C \epsilon_S(\nu_C) \ln\Lambda \tag{56}$$

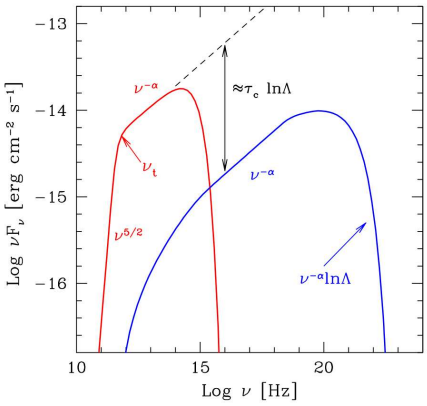

Figure 8: Example of SSC spectrum. The plot is in the νF_ν representation while the spectral indices correspond to the $F_\nu \propto \nu^\alpha$ convention (adapted from Ghisellini, 2013a).

Appendix C Modeling

In order to extract the physical parameters associated with the powerful emission of blazars, modeling the observed fluxes in the νF_ν diagram is required.

The major blazars model are: leptonic models (e.g., Ghisellini & Tavecchio, 2009; Moderski et al., 2003) and hadronic models (e.g., Böttcher et al., 2013; Mannheim, 1998). Leptonic models have been successful in explaining many feature in the spectral energy distribution (SED) of blazars and are the most used in the available literature.

In this work we have adopted a time independent leptonic emission model using the sources available in the literature (see e.g., Dermer et al., 2009; Finke et al., 2008; Ghisellini & Tavecchio, 2009). In this Appendix we briefly describe the model. Details can be found in the cited papers.

C.1 Emission region

The observed radiation is assumed to originate from a spherical emission region covering the entire cross-section of the jet, located at a distance of $R_{\rm diss}$ from the central engine, and moving with the bulk Lorentz factor Γ which is assumed to be constant

The jet semi opening angle (ψ) is assumed to be 0.1 rad. The relativistic electron population is assumed to follow a smooth broken power law energy distribution

$$N(\gamma) \propto \frac{(\gamma_{\rm break})^{-p}}{(\gamma/\gamma_{\rm break})^{p} + (\gamma/\gamma_{\rm break})^{q}}. \tag{57}$$

where $\gamma_{\rm break}$ is the break energy, p and q are the slopes of the particle energy distribution before and after $\gamma_{\rm break}$, respectively.

C.2 Energy Densities

C.2.1 Disk Radiation

The emission from the disk is modeled assuming a standard optically thick, geometrically thin disk (Shakura & Sunyaev, 1973). Assuming an accretion rate $\dot{M}$ and an efficiency η_{acc}, the disk luminosity can be expressed as $L_{disk} = \eta_{\rm acc}\dot{M}c^2$. Locally, the radiation is assumed to be produced by annular rings each emitting as a blackbody with a specific temperature. The radiative profile of the accretion disk is considered as a multi-temperature blackbody of the form (see e.g., Frank et al., 2002)

$$T(R) = \frac{3R_{\rm Sch}L_{\rm disk}}{16\pi\eta_{\rm a}\sigma_{\rm SB}R^3}\left[1-\left(\frac{3R_{\rm Sch}}{R}\right)^{1/2}\right]^{1/4}, \tag{58}$$

The inner radius of the accretion disk is assumed as $R_{\rm in} = 3R_{\rm Sch}$ and the outer radius $R_{\rm out} = 500R_{\rm Sch}$. Due to differet temperatures and angles with respect to the jet axis (ϕ), the radiation from each ring is amplified in a different way. In the lab frame (stationary observer with respect to the black hole) will see a flux, integrated over all annuli, of (see, Ghisellini & Tavecchio, 2009)

$$F_d = 2\pi\int_{\mu_1}^{\mu_2} I(\nu)d\mu = 2\pi\int_{\mu_1}^{\mu_2}\frac{2h\nu^3/c^2}{exp[h\nu/kT]-1}d\mu \tag{59}$$

where $\mu = \cos\theta$, and μ_1 and μ_2 are given by

$$\mu_1 = [1+R_{\rm out}^2/R_{\rm diss}^2]^{-1/2} \qquad \mu_2 = [1+R_{\rm in}^2/R_{\rm diss}^2]^{-1/2} \tag{60}$$

The specific radiation density seen in the comoving frame (see Appendix A for angle transformations) is

$$U_d'(\nu') = \frac{1}{c}\int I_d'(\nu')d\Omega' = \frac{2\pi}{c}\int_{\mu_d}^{1} I_d'(\nu')b^2 d\mu \tag{61}$$

where $b = 1/\delta$. Integrating Eq. 61 over all frequencies gives the total accretion disk energy density as a function of $R_{\rm diss}$.

C.2.2 Hot Corona emission

Above and below the accretion disk lies the X-ray corona. This reprocesses radiation from the accretion disk by Compton-scattering (efficiency $\eta_{\rm cor}$). The emission spectrum of the corona is assumed to be a cut-off powerlaw:

$$L_{\rm cor}(\epsilon) \propto \epsilon^{-\alpha_{\rm cor}} \exp(-\epsilon/\epsilon_C) \tag{62}$$

where ϵ is the dimensionless photon energy.

The total radiation energy density is given by (see, Ghisellini & Madau, 1996)

$$\begin{aligned} U'_{\rm cor} &= \frac{\eta_{\rm cor} L_{\rm disk} \Gamma^2}{\pi R_X^2 c} [1 - \mu_X - \beta(1-\mu_X^2) + \beta^2 3(1-\mu_X^3)] \\ \mu_X &= [1 + R_{\rm X}^2/R_{\rm diss}^2]^{-1/2} \end{aligned} \tag{63}$$

The inner radius of the accretion disk is assumed as $R_{\rm in} = 3R_{\rm Sch}$ and the outer radius $R_{\rm out} = 30R_{\rm Sch}$. $R_{\rm X}$ is the extension of the X-ray corona.

C.2.3 BLR radiation

The BLR is assumed to be a spherical shell located at $R_{\rm BLR} = 10^{17} L_{\rm disk,45}^{1/2}$ cm, where $L_{\rm disk,45}$ is the accretion disk luminosity in units of 10^{45} erg s^{-1}(see, Ghisellini & Tavecchio, 2009). Its spectrum is considered to be a blackbody peaking at rest-frame Lyman-α frequency (Tavecchio & Ghisellini, 2008) and it reprocesses $\eta_{\rm BLR}$ of the disk radiation. The BLR energy density seen in the comoving frame can be approximated as

(see, Ghisellini & Madau, 1996)

$$
\begin{aligned}
U'_{\rm BLR} &\sim \frac{17\Gamma^2}{12}\frac{\eta_{\rm BLR}L_{\rm disk}}{4\pi R^2_{\rm BLR}c} \qquad\qquad R_{\rm diss} < R_{\rm BLR} \\
U'_{\rm BLR} &\sim \frac{\Gamma^2}{3\beta}\frac{\eta_{\rm BLR}L_{\rm disk}}{4\pi R^2_{\rm BLR}c}[2(1-\beta\mu_1)^3 - (1-\beta\mu_2)^3 - (1-\beta)^3] \qquad R_{\rm diss} \gg R_{\rm BLR} \\
\mu_1 &= [1 + R^2_{\rm BLR}/R^2_{\rm diss}]^{-1/2} \\
\mu_2 &= [1 - R^2_{\rm BLR}/R^2_{\rm diss}]^{-1/2}
\end{aligned}
\tag{64}
$$

In the range $R_{\rm BLR} < R_{\rm diss} < 3R_{\rm BLR}$ a simple powerlaw interpolation is adopted as the exact value of $U_{\rm BLR}$ depends on the width of the region, which is not well understood.

C.2.4 Torus Emission

Like the BLR, the torus is assumed to be a spherical shell located at a distance $R_{\rm IR} = 10^{18}L^{1/2}_{\rm disk,45}$ cm from the accretion disk. It reprocesss $\eta_{\rm torus}$ of the disk emission. Its emission profile is a blackdoby peaking at $T_{\rm torus}$. The comoving radiation energy density of the IR-torus have the same profile as $U_{\rm BLR}$:

$$
\begin{aligned}
U'_{\rm torus} &\sim \frac{\eta_{\rm torus}L_{\rm disk}\Gamma^2}{4\pi R^2_{\rm torus}c} \qquad\qquad R_{diss} < R_{torus} \\
U'_{\rm torus} &\sim \frac{\Gamma^2}{3\beta}\frac{\eta_{\rm torus}L_{\rm disk}\Gamma^2}{4\pi R^2_{\rm torus}c}[2(1-\beta\mu_1)^3 - (1-\beta\mu_2)^3 - (1-\beta)^3] \qquad R_{\rm diss} \gg R_{\rm torus} \\
\mu_1 &= [1 + R^2_{\rm torus}/R^2_{\rm diss}]^{-1/2} \\
\mu_2 &= [1 - R^2_{\rm torus}/R^2_{\rm diss}]^{-1/2}
\end{aligned}
\tag{65}
$$

C.2.5 Magnetic Energy Density

The magnetic energy density can be expressed as

$$
U'_B = \frac{P_{\rm B}}{\pi R^2_{\rm blob}\Gamma^2 c} \tag{66}
$$

where $P_{\rm B}$ is the power carried in the form of Poynting flux.

In Figure 9 we report the contributions to the energy density provided by the different components as a function of $R_{\rm diss}$.

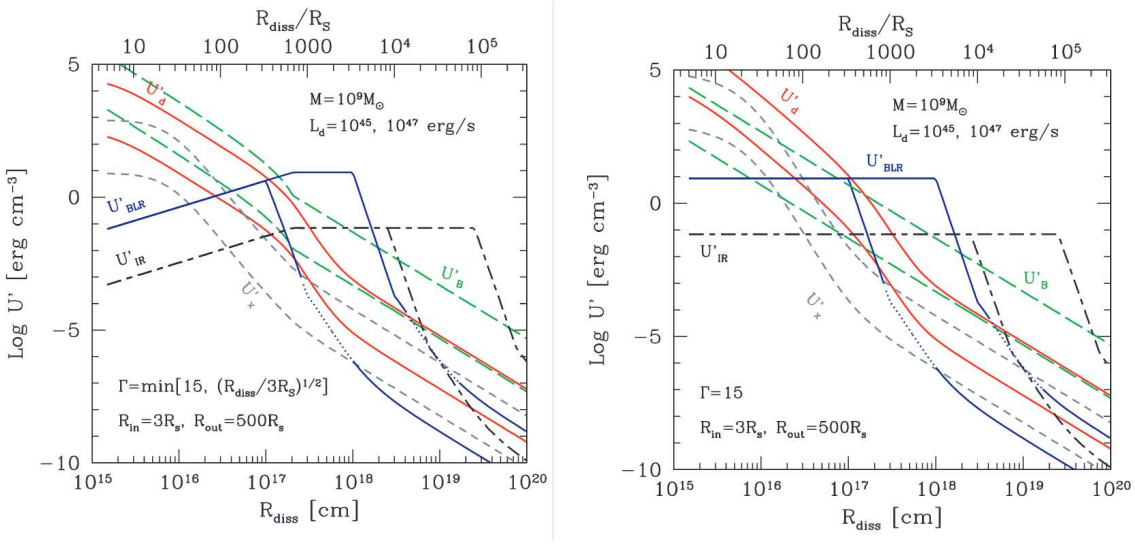

Figure 9: Left panel(a): comparison of different energy densities as measured in the comoving frame. The bulk Lorentz factor is assumed to scale as $\Gamma = \min[\Gamma_{\rm max}, (\frac{R}{3R_{\rm Sch}})^{1/2}]$. The black hole mass is assumed $\gtrsim 10^9 M_\odot$. The two sets of lines correspond to disc luminosities of 10^45 and 10^47 erg s^{-1}. The radius of the BLR and the IR torus are given as $R_{\rm BLR} = 10^{17} L_{\rm disk,45}^{1/2}$ cm, and $R_{\rm torus} = 10^{18} L_{\rm disk,45}^{1/2}$ cm, respectively. The magnetic energy density (long dashed lines) is calculated assuming $P_{\rm B} = 0.1 L_{\rm disk}$. Right panel(b): same plot as the left panel, but Γ is considered constant with value 15. (adapted from (Ghisellini & Tavecchio, 2009))

C.3 Synchrotron Radiation

For our purposes, we utilize the synchrotron flux from isotropic electrons, moving in a randomly oriented magnetic field as reported in Finke et al., 2008:

$$f_\epsilon^{\rm sync} = \frac{\delta_D^4 \epsilon' J'_{\rm sync}(\epsilon')}{4\pi d_L^2} = \frac{\sqrt{3}\delta_D^4 \epsilon' e^3 B}{4\pi h d_L^2} \int_1^\infty d\gamma' N'_e(\gamma') R(x) \tag{67}$$

where

$$R(x) \approx 1.78 x^{0.297} \exp(-\mathrm{x})$$
$$x = \frac{4\pi\epsilon' m_e^2 c^3}{3eBh\gamma'^2} \tag{68}$$

C.3.1 Synchrotron Self Absorption

The synchrotron self absorption (SSA) coefficient is calculated following Dermer & Menon, 2009:

$$\kappa'(\epsilon') = -\frac{1}{8\pi m_e \epsilon'^2}\left(\frac{\lambda_C}{c}\right)^3\left(\frac{\delta_D}{(1+z)}\right)^2\int_{\gamma'_{min}}^{\gamma'_{max}} d\gamma' P^{\mathrm{sync}}(\epsilon';\gamma')[\gamma'^2]\frac{\partial}{\partial\gamma'}\left(\frac{n'_e(\gamma')}{\gamma'^2}\right) \tag{69}$$

where $\lambda_C = h/m_e c$ is the Compton wavelength and $n'_e(\gamma') = N'_e(\gamma')/V'_{blob}$. The optical depth for SSA is $\tau_{\epsilon'} = 2\kappa'(\epsilon')R'_{blob}$. The unabsorbed spectrum has to be multiplied by a factor $3u(\tau_{\epsilon'})/\tau_{\epsilon'}$ to obtain the absorbed one (Gould, 1979) with $u(\tau_{\epsilon'})$ expressed as

$$u(\tau_{\epsilon'}) = \frac{1}{2} + \frac{\exp(-\tau_{\epsilon'})}{\tau_{\epsilon'}} - \frac{1-\exp(-\tau_{\epsilon'})}{\tau^2_{\epsilon'}} \tag{70}$$

C.3.2 Synchrotron Self Compton

The single particle SSC emissivity, integrated over volume, for isotropic and homogeneous photon and electron energy distribution is (see, Finke et al., 2008):

$$\epsilon'_{\mathrm{S}} J'_{\mathrm{SSC}} = \frac{3}{4} c\sigma_T \epsilon'^2_{\mathrm{S}} \int_0^\infty d\epsilon' \frac{u'(\epsilon')}{\epsilon'^2}\int_{\gamma'_{min}}^{\gamma'_{max}} d\gamma' \frac{N'_e(\gamma')}{\gamma'^2} F_{\mathrm{C}}(q,\Gamma_e) \tag{71}$$

where ϵ'_{S} is the dimensionless energy of the scattered photon in the blob frame and $F_{\mathrm{C}}(q,\Gamma_e)$ is the Compton scattering kernel, which takes into account both the Thomson and Klein-Nishina regimes. Details on the behaviour of $F_C(q,\Gamma_e)$ can be found in Blumenthal & Gould, 1970; Jones, 1968.

The SSC spectrum is given by (see, Dermer & Menon, 2009; Finke et al., 2008):

$$\begin{aligned} f_{\epsilon_{\rm S}}^{\rm SSC} &= \frac{\delta_D^4 \epsilon'_{\rm S} J'_{\rm SSC}(\epsilon'_{\rm S})}{4\pi d_L^2} \\ &= \frac{9\sigma_T \epsilon_{\rm S}^{'2}}{16\pi R_{\rm blob}^{'2}} \int_0^\infty d\epsilon' \frac{f_\epsilon^{\rm syn}}{\epsilon^{'3}} \int_{\gamma'_{min}}^{\gamma'_{max}} d\gamma' \frac{N'_e(\gamma')}{\gamma^{'2}} F_{\rm C}(q, \Gamma_e) \end{aligned} \tag{72}$$

C.4 External Compton Radiation

For an isotropic comoving distribution of electrons and external photons, assuming head-on collision, the Compton νF_ν spectrum is given by (Dermer & Menon, 2009)

$$f_{\epsilon_{\rm S}}^{\rm EC} = \frac{3c\sigma_T \epsilon_S^{'2} \delta_D^4}{16\pi d_L^2} \int_0^\infty d\epsilon' \frac{u'(\epsilon')}{\epsilon^{'2}} \int_{\gamma'_{min}}^{\gamma'_{max}} d\gamma' \frac{N'_e(\gamma')}{\gamma^{'2}} F_{\rm C}(q, \Gamma_e) \tag{73}$$

where $u'(\epsilon')$ is the external specific photon energy density measured in the comoving frame. As long as the emission in within the BLR, all external photons appear to arrive at the same angle ($\theta_v = 1/\Gamma$) and the observed luminosity in the rest frame is isotropic. If the emitting region is instead outside the BLR the incoming photons arrive from different directions and it is difficult to reproduce the exact emission. For simplicity the assumption $\theta_v \sim 1/\Gamma$ holds and the emitted radiation patter is treated as for an isotropic seed photon distribution.

Both the BLR and IR-torus energy densities can be written as (Rybicki & Lightman, 1986):

$$u'_{ext}(\epsilon') = \frac{15 u'_{tot}}{(\pi\Theta')^4} \left[\frac{\epsilon'^3}{exp(\epsilon'/\Theta') - 1} \right] \tag{74}$$

where $\Theta' = k_B T'/m_e c^2$ is the dimensionless temperature with k_B Boltzmann constant. The spectrum in the observer's frame would be:

$$f_{\epsilon_{\rm S}}^{EC} = \frac{3c\sigma_T \epsilon_S^{'2} \delta_D^4}{16\pi d_L^2} \frac{15 u'_{ext}}{(\pi\Theta')^4} \int_0^\infty d\epsilon' \frac{\epsilon'}{exp(\epsilon'/\Theta') - 1} \int_{\gamma'_{min}}^{\gamma'_{max}} d\gamma' \frac{N'_e(\gamma')}{\gamma^{'2}} F_{\rm C}(q, \Gamma_e) \tag{75}$$

In the comoving frame the photon energy is $\epsilon'_{peak} \sim \Gamma \epsilon_{peak}$ and the external photon energy density is given by $u'_{ext} \sim \Gamma u_{ext}$.

Bibliography

Abdo, A. A., Ackermann, M., Agudo, I., et al. 2010, ApJ, 716, 30

Acero, F., Ackermann, M., Ajello, M., et al. 2015, ApJS, 218, 23

Acero, F., Ackermann, M., Ajello, M., et al. 2016, The Astrophysical Journal Supplement Series, 223, 26. http://stacks.iop.org/0067-0049/223/i=2/a=26

Ackermann, M., Ajello, M., Ballet, J., et al. 2012, ApJ, 751, 159

Ackermann, M., Ajello, M., Albert, A., et al. 2013, ApJ, 771, 57

Ackermann, M., Ajello, M., Baldini, L., et al. 2017, The Astrophysical Journal Letters, 837, L5. http://stacks.iop.org/2041-8205/837/i=1/a=L5

Aihara, H., Allende Prieto, C., An, D., et al. 2011, ApJS, 193, 29

Ajello, M., Costamante, L., Sambruna, R. M., et al. 2009, ApJ, 699, 603

Ajello, M., Gasparrini, D., Sánchez-Conde, M., et al. 2015, ApJ, 800, L27

Ajello, M., Ghisellini, G., Paliya, V. S., et al. 2016, ApJ, 826, 76

Antonucci, R. 1993, ARA&A, 31, 473

Atwood, W., Albert, A., Baldini, L., et al. 2013, arXiv:1303.3514, arXiv:1303.3514

Atwood, W. B., Abdo, A. A., Ackermann, M., et al. 2009, ApJ, 697, 1071

Balick, B., & Brown, R. L. 1974, ApJ, 194, 265

Ballabriga, R., Alozy, J., Campbell, M., et al. 2016, Journal of Instrumentation, 11, P01007. http://stacks.iop.org/1748-0221/11/i=01/a=P01007

Barthelmy, S. D., Barbier, L. M., Cummings, J. R., et al. 2005, Space Sci. Rev., 120, 143

Beckmann, V., & Shrader, C. R. 2012, Active Galactic Nuclei

Begelman, M. C. 2014, ArXiv e-prints, arXiv:1410.8132

Begelman, M. C., Blandford, R. D., & Rees, M. J. 1984, Reviews of Modern Physics, 56, 255

Begelman, M. C., & Sikora, M. 1987, ApJ, 322, 650

Biretta, J. A., Sparks, W. B., & Macchetto, F. 1999, The Astrophysical Journal, 520, 621. http://stacks.iop.org/0004-637X/520/i=2/a=621

Blandford, R. D., & Payne, D. G. 1982, MNRAS, 199, 883

Blandford, R. D., & Rees, M. J. 1978, Phys. Scr, 17, 265

Blandford, R. D., & Znajek, R. L. 1977, MNRAS, 179, 433

Błażejowski, M., Sikora, M., Moderski, R., & Madejski, G. M. 2000, ApJ, 545, 107

Bloemen, H., Bennett, K., Blom, J. J., et al. 1995, A&A, 293

Blumenthal, G. R., & Gould, R. J. 1970, Reviews of Modern Physics, 42, 237

Böttcher, M., Reimer, A., & Zhang, H. 2013, in European Physical Journal Web of Conferences, Vol. 61, European Physical Journal Web of Conferences, 05003

Burrows, D. N., Hill, J. E., Nousek, J. A., et al. 2005, Space Sci. Rev., 120, 165

Cash, W. 1979, ApJ, 228, 939

Celotti, A., & Ghisellini, G. 2008, MNRAS, 385, 283

Celotti, A., Ghisellini, G., & Fabian, A. C. 2007, MNRAS, 375, 417

Citterio, O., Campano, S., Conconi, P., et al. 1996, in Proc. SPIE, Vol. 2805, Multilayer and Grazing Incidence X-Ray/EUV Optics III, ed. R. B. Hoover & A. B. Walker, 56–65

Collmar, W. 2006, in Astronomical Society of the Pacific Conference Series, Vol. 350, Blazar Variability Workshop II: Entering the GLAST Era, ed. H. R. Miller, K. Marshall, J. R. Webb, & M. F. Aller, 120

De Angelis, A., Tatischeff, V., Tavani, M., et al. 2016, ArXiv e-prints, arXiv:1611.02232

Dermer, C. D., Finke, J. D., Krug, H., & Böttcher, M. 2009, ApJ, 692, 32

Dermer, C. D., & Giebels, B. 2016, Comptes Rendus Physique, 17, 594

Dermer, C. D., & Menon, G. 2009, High Energy Radiation from Black Holes: Gamma Rays, Cosmic Rays, and Neutrinos, Princeton University Press

Dermer, C. D., & Schlickeiser, R. 1993, ApJ, 416, 458

Falomo, R., Scarpa, R., Treves, A., & Urry, C. M. 2000, ApJ, 542, 731

Fath, E. A. 1909, Lick Observatory Bulletin, 5, 71

Finke, J. D., Dermer, C. D., & Böttcher, M. 2008, ApJ, 686, 181

Forman, W., Jones, C., Cominsky, L., et al. 1978, ApJS, 38, 357

Fossati, G., Celotti, A., Ghisellini, G., & Maraschi, L. 1999, in Astronomical Society of the Pacific Conference Series, Vol. 159, BL Lac Phenomenon, ed. L. O. Takalo & A. Sillanpää, 351

Fossati, G., Maraschi, L., Celotti, A., Comastri, A., & Ghisellini, G. 1998, MNRAS, 299, 433

Frank, J., King, A., & Raine, D. J. 2002, Accretion Power in Astrophysics, by Juhan Frank and Andrew King and Derek Raine, pp. 398. ISBN 0521620538. Cambridge, UK: Cambridge University Press, February 2002

Fricke, K. J., Kollatschny, W., & Witzel, A. 1983, A&A, 117, 60

Gehrels, N., Chipman, E., & Kniffen, D. A. 1993, A&AS, 97, 5

Gehrels, N., Chincarini, G., Giommi, P., et al. 2004, ApJ, 611, 1005

Ghez, A. M., Klein, B. L., Morris, M., & Becklin, E. E. 1998, ApJ, 509, 678

Ghisellini, G., ed. 2013a, Lecture Notes in Physics, Berlin Springer Verlag, Vol. 873, Radiative Processes in High Energy Astrophysics

Ghisellini, G. 2013b, Mem. Soc. Astron. Italiana, 84, 719

Ghisellini, G. 2016, Galaxies, 4

Ghisellini, G., Celotti, A., Fossati, G., Maraschi, L., & Comastri, A. 1998, MNRAS, 301, 451

Ghisellini, G., & Madau, P. 1996, MNRAS, 280, 67

Ghisellini, G., & Tavecchio, F. 2009, MNRAS, 397, 985

—. 2010, MNRAS, 409, L79

—. 2015, MNRAS, 448, 1060

Ghisellini, G., Tavecchio, F., Maraschi, L., Celotti, A., & Sbarrato, T. 2014, Nature, 515, 376

Ghisellini, G., Della Ceca, R., Volonteri, M., et al. 2010, MNRAS, 405, 387

Giacconi, R., & Gursky, H., eds. 1974, Astrophysics and Space Science Library, Vol. 43, X-ray astronomy

Giacconi, R., Gursky, H., Paolini, F. R., & Rossi, B. B. 1962, Physical Review Letters, 9, 439

Gould, R. J. 1979, A&A, 76, 306

Greenstein, J. L., & Matthews, T. A. 1963, AJ, 68, 279

Greiner, J., Bornemann, W., Clemens, C., et al. 2008, PASP, 120, 405

Harrison, F., & HEX-P Collaboration Collaboration. 2017, in APS April Meeting Abstracts

Harrison, F. A., Craig, W. W., Christensen, F. E., et al. 2013, ApJ, 770, 103

Hazard, C., Mackey, M. B., & Shimmins, A. J. 1963, Nature, 197, 1037

Jansky, K. G. 1933, Nature, 132, 66

Johnson, J. L., & Haardt, F. 2016, PASA, 33, e007

Jones, F. C. 1968, Physical Review, 167, 1159

Kalberla, P. M. W., Burton, W. B., Hartmann, D., et al. 2005, A&A, 440, 775

Kellermann, K. I., Sramek, R., Schmidt, M., Shaffer, D. B., & Green, R. 1989, AJ, 98, 1195

Komatsu, E., Dunkley, J., Nolta, M. R., et al. 2009, ApJS, 180, 330

Konigl, A. 1981, ApJ, 243, 700

Kormendy, J., & Richstone, D. 1995, ARA&A, 33, 581

Krühler, T., Küpcü Yoldaş, A., Greiner, J., et al. 2008, ApJ, 685, 376

Madsen, K. K., Harrison, F. A., Markwardt, C. B., et al. 2015, ApJS, 220, 8

Mannheim, K. 1998, Science, 279, 684

Marcotulli, L., Paliya, V. S., Ajello, M., et al. 2017, ArXiv e-prints, arXiv:1703.10657

Mattox, J. R., Bertsch, D. L., Chiang, J., et al. 1996, ApJ, 461, 396

Moderski, R., Sikora, M., & Błażejowski, M. 2003, A&A, 406, 855

Nenkova, M., Ivezić, Ž., & Elitzur, M. 2002, ApJ, 570, L9

O'Dowd, M., Urry, C. M., & Scarpa, R. 2002, ApJ, 580, 96

Paliya, V. S., Parker, M. L., Fabian, A. C., & Stalin, C. S. 2016, ApJ, 825, 74

Pjanka, P., Zdziarski, A. A., & Sikora, M. 2017, Monthly Notices of the Royal Astronomical Society, 465, 3506. +http://dx.doi.org/10.1093/mnras/stw2960

Pudritz, R. E., Hardcastle, M. J., & Gabuzda, D. C. 2012, Space Sci. Rev., 169, 27

Reber, G. 1944, ApJ, 100, 279

Rees, M. J. 1974, The Observatory, 94, 168

—. 1984, ARA&A, 22, 471

Romani, R. W., Sowards-Emmerd, D., Greenhill, L., & Michelson, P. 2004, ApJ, 610, L9

Roming, P. W. A., Kennedy, T. E., Mason, K. O., et al. 2005, Space Sci. Rev., 120, 95

Rybicki, G. B., & Lightman, A. P. 1986, Radiative Processes in Astrophysics, 400

Sambruna, R. M., Markwardt, C. B., Mushotzky, R. F., et al. 2006, ApJ, 646, 23

Sbarrato, T., Ghisellini, G., Maraschi, L., & Colpi, M. 2012, MNRAS, 421, 1764

Sbarrato, T., Tagliaferri, G., Ghisellini, G., et al. 2013, ApJ, 777, 147

Schlafly, E. F., & Finkbeiner, D. P. 2011, ApJ, 737, 103

Schmidt, M. 1965, in Quasi-Stellar Sources and Gravitational Collapse, ed. I. Robinson, A. Schild, & E. L. Schucking, 455

Seyfert, C. K. 1943, ApJ, 97, 28

Shakura, N. I., & Sunyaev, R. A. 1973, A&A, 24, 337

Shaw, M. S., Romani, R. W., Cotter, G., et al. 2012, ApJ, 748, 49

Shen, Y., Richards, G. T., Strauss, M. A., et al. 2011, ApJS, 194, 45

Shields, G. A. 1978, Nature, 272, 706

Sikora, M., Begelman, M. C., & Rees, M. J. 1994, ApJ, 421, 153

Sikora, M., Madejski, G., Moderski, R., & Poutanen, J. 1997, ApJ, 484, 108

Sikora, M., Rutkowski, M., & Begelman, M. C. 2016, MNRAS, 457, 1352

Sironi, L., Keshet, U., & Lemoine, M. 2015, Space Sci. Rev., 191, 519

Skrutskie, M. F., Cutri, R. M., Stiening, R., et al. 2006, AJ, 131, 1163

Southworth, G. 1945, Journal of the Franklin Institute, 239, 285 . http://www.sciencedirect.com/science/article/pii/0016003245901633

Stickel, M., Padovani, P., Urry, C. M., Fried, J. W., & Kuehr, H. 1991, ApJ, 374, 431

Stocke, J. T., Morris, S. L., Gioia, I. M., et al. 1991, ApJS, 76, 813

Tagliaferri, G., Ghisellini, G., Perri, M., et al. 2015, ApJ, 807, 167

Tavecchio, F., & Ghisellini, G. 2008, MNRAS, 386, 945

Thompson, D. J., Bertsch, D. L., Fichtel, C. E., et al. 1993, ApJS, 86, 629

Urry, C. M., & Padovani, P. 1995, PASP, 107, 803

Vanden Berk, D. E., Richards, G. T., Bauer, A., et al. 2001, AJ, 122, 549

Vestergaard, M., & Peterson, B. M. 2006, ApJ, 641, 689

Wehrle, A. E., Piner, B. G., Unwin, S. C., et al. 2001, ApJS, 133, 297

Willmore, A. P. 1970, in IAU Symposium, Vol. 37, Non-Solar X- and Gamma-Ray Astronomy, ed. L. Gratton, 50

Wood, K. S., Meekins, J. F., Yentis, D. J., et al. 1984, ApJS, 56, 507

Zombeck, M. V. 1990, Handbook of space astronomy and astrophysics